The Astrophysical Journal, 782:6 (22pp), 2014 February 10 doi:10.1088/0004-637X/782/1/6

THE LYMAN ALPHA REFERENCE SAMPLE. II. *HUBBLE SPACE TELESCOPE* IMAGING RESULTS, INTEGRATED PROPERTIES, AND TRENDS*

Matthew Hayes[1,2,3], Göran Östlin[1], Florent Duval[1], Andreas Sandberg[1], Lucia Guaita[1], Jens Melinder[1], Angela Adamo[4], Daniel Schaerer[2,5], Anne Verhamme[5], Ivana Orlitová[5,6], J. Miguel Mas-Hesse[7], John M. Cannon[8], Hakim Atek[9], Daniel Kunth[10], Peter Laursen[11], Héctor Otí-Floranes[7,12,13], Stephen Pardy[8], Thøger Rivera-Thorsen[1], and E. Christian Herenz[14]
[1] Department of Astronomy, Oskar Klein Centre, Stockholm University, AlbaNova University Centre, SE-106 91 Stockholm, Sweden; matthew@astro.su.se
[2] Université de Toulouse, UPS-OMP, IRAP, F-31000 Toulouse, France
[3] CNRS, IRAP, 14 Avenue Edouard Belin, F-31400 Toulouse, France
[4] Max Planck Institute for Astronomy, Königstuhl 17, D-69117 Heidelberg, Germany
[5] Geneva Observatory, University of Geneva, 51 Chemin des Maillettes, CH-1290 Versoix, Switzerland
[6] Astronomical Institute, Academy of Sciences of the Czech Republic, Boční II, CZ-14131 Prague, Czech Republic
[7] Centro de Astrobiología (CSIC–INTA), Departamento de Astrofísica, P.O. Box 78, E-28691 Villanueva de la Cañada, Spain
[8] Department of Physics and Astronomy, Macalester College, 1600 Grand Avenue, Saint Paul, MN 55105, USA
[9] Laboratoire dAstrophysique, École Polytechnique Fédérale de Lausanne (EPFL), Observatoire, CH-1290 Sauverny, Switzerland
[10] Institut d'Astrophysique de Paris, UMR 7095, CNRS and UPMC, 98 bis Bd Arago, F-75014 Paris, France
[11] Dark Cosmology Centre, Niels Bohr Institute, University of Copenhagen, Juliane Maries Vej 30, DK-2100 Copenhagen, Denmark
[12] Instituto de Astronomía, Universidad Nacional Autónoma de México, Apdo. Postal 106, Ensenada B. C. 22800, Mexico
[13] Dpto. de Física Moderna, Facultad de Ciencias, Universidad de Cantabria, E-39005 Santander, Spain
[14] Leibniz-Institut für Astrophysik (AIP), An der Sternwarte 16, D-14482 Potsdam, Germany
Received 2013 July 17; accepted 2013 December 10; published 2014 January 20

ABSTRACT

We report new results regarding the Lyα output of galaxies, derived from the *Lyman Alpha Reference Sample*, and focused on *Hubble Space Telescope* imaging. For 14 galaxies we present intensity images in Lyα, Hα, and UV, and maps of Hα/Hβ, Lyα equivalent width (EW), and Lyα/Hα. We present Lyα and UV radial light profiles and show they are well-fitted by Sérsic profiles, but Lyα profiles show indices systematically lower than those of the UV ($n \approx 1$–2 instead of $\gtrsim$4). This reveals a general lack of the central concentration in Lyα that is ubiquitous in the UV. Photometric growth curves increase more slowly for Lyα than the far ultraviolet, showing that small apertures may underestimate the EW. For most galaxies, however, flux and EW curves flatten by radii $\approx$10 kpc, suggesting that if placed at high-z only a few of our galaxies would suffer from large flux losses. We compute global properties of the sample in large apertures, and show total Lyα luminosities to be independent of all other quantities. Normalized Lyα throughput, however, shows significant correlations: escape is found to be higher in galaxies of lower star formation rate, dust content, mass, and nebular quantities that suggest harder ionizing continuum and lower metallicity. Six galaxies would be selected as high-z Lyα emitters, based upon their luminosity and EW. We discuss the results in the context of high-z Lyα and UV samples. A few galaxies have EWs above 50 Å, and one shows $f_{\rm esc}^{\rm Ly\alpha}$ of 80%; such objects have not previously been reported at low-z.

Key words: cosmology: observations – galaxies: starburst

Online-only material: color figures

1. INTRODUCTION

The Lyman Alpha Reference Sample (LARS; G. Östlin et al., in preparation, hereafter Paper I) is a sample of 14 nearby star-forming galaxies, selected for observation with the *Hubble Space Telescope* (*HST*) and an array of other telescopes. The primary goals are to return detailed observations—both in images and spectra—of the H I Lyα emission line, and to do so in a sample that is simultaneously as free from bias as possible, statistically meaningful enough to observe trends within the sample, and comparable in selection to galaxies observed in the high-z universe. With as much information about the emitted Lyα as possible, the data set is then completed by amassing as much information on the stars, and various phases of the interstellar medium (ISM) as possible; from these we measure and map the properties of the galaxies, their intrinsic Lyα, and the properties of the medium through which the Lyα must travel in order to escape and reach the observer.

The astrophysical motivation for LARS is straightforward: Lyα is intrinsically the most luminous feature in the spectrum of a hot source (Schaerer 2003; Raiter et al. 2010), and was recognized almost half a century ago as a potential beacon through which to study the distant universe (Partridge & Peebles 1967). However while intrinsically very luminous in Lyα the fact that Lyα scatters wherever it encounters H I gas means that it may encode not only information about the nebulae in which it was produced, but also the interstellar, circumgalactic, and intergalactic media (IGM) through which it must have transferred. This radiative transport modifies the spectral distributions of the Lyα radiation, typically resulting in the observed asymmetric line profiles (Kunth et al. 1998; Rhoads et al. 2003; Shapley et al. 2003; Shimasaku et al. 2006; Tapken et al. 2007; Vanzella et al. 2010; Lidman et al. 2012; Wofford

* Based on observations made with the NASA/ESA *Hubble Space Telescope*, obtained at the Space Telescope Science Institute, which is operated by the Association of Universities for Research in Astronomy, Inc., under NASA contract NAS 5-26555. These observations are associated with program No.12310.

et al. 2013) or double peaks (Shapley et al. 2006; Quider et al. 2009; Heckman et al. 2011; Kulas et al. 2012; Yamada et al. 2012), and spatially extended Lyα emission (Fynbo et al. 2001; Steidel et al. 2003, 2011; Hayes et al. 2005, 2007; Östlin et al. 2009; Matsuda et al. 2012).

The Lyα output from galaxies has been shown to evolve strongly with redshift (Hayes et al. 2011; Stark et al. 2011; Schaerer et al. 2011; Blanc et al. 2011; Dijkstra & Jeeson-Daniel 2013) in a fashion that, in contrast to the star formation rate (SFR) density (e.g., Hopkins & Beacom 2006), is completely monotonic. Naturally this phenomenon must reflect a fundamental change in the galaxy population, but currently the Lyα emissivity is little more than an indicator. If we are to use Lyα to study the high-z galaxy population, and for example as a probe of cosmic reionization (e.g., Haiman & Spaans 1999; Santos 2004; Malhotra & Rhoads 2004; Kashikawa et al. 2006; Dijkstra et al. 2007), we need to understand under what conditions galaxies become strong Lyα emitters. In doing so, we must simultaneously try to account for aperture losses that may result from Lyα scattering, as low surface brightness haloes may, or may not (Feldmeier et al. 2013) be ubiquitous. This can only be achieved by assembling a data set that comprises a sufficiently large sample of galaxies, and observations that measure all the quantities thought to be complicit in the Lyα transport process. This second requirement also sets a limit on redshift: it must be low enough to enable us to study galaxies in detail, and probe the scattering medium directly. It was precisely to this end that the LARS survey was designed—Paper I gives a complete overview of the survey, motivations, and sample selection.

The backbone of LARS is an *HST* ultraviolet (UV) and optical imaging campaign, carried out with the Advanced Camera for Surveys (ACS) and Wide Field Camera 3 (WFC3). The observational parameters of the survey are described in Paper I. This enables us to map the Lyα emission and absorption on spatial scales as low as 30 pc, and also determine the properties of the stellar population and nebular gas, including the dust attenuation, in both phases on the same scales. Additional campaigns include *HST* UV spectroscopy in Lyα and the nearby continuum, 21 cm line observations of the H I, three-dimensional spectroscopy and narrowband imaging in more nebular emission lines, and all of these data sets will provide the subject of forthcoming papers.

In this paper we present the first set of "global" results that can be obtained from the *HST* imaging observations. In Hayes et al. (2013) we showed the first images in Lyα, Hα, and the UV continuum, and quantified the extent of Lyα emission and compared it with the other hot stellar and nebular radiation. In this paper we take that analysis a lot further and present a library of individual intensity images, and maps of line ratios and equivalent widths (EWs). We also present aperture growth curves to examine the recovered quantities as a function of aperture size, and global properties of the sample, computed in homogeneously defined apertures, in order to examine global trends in the Lyα throughput. Generally, Sections 2–5 describe the data, while Sections 6–8 discuss its astrophysical meaning.

In Section 2 we present a brief overview of the imaging data. In Section 3 we present images in Lyα and other relevant wavelengths (Hα and far-ultraviolet (FUV) continuum) and discuss line ratios and EW maps. In Section 4 we show the spatial distribution of Lyα and related observables, both as radial surface brightnesses and the integrated quantities in collapsed apertures. In Section 5 we measure some global properties, and show how the Lyα output of the sample may depend upon various inferable stellar and nebular quantities, and in Section 6 we point out interesting and relevant features in the individual targets, and discuss their properties. Section 7 describes the "analog" nature of the sample and discusses how LARS galaxies would conform to high-z UV and Lyα selection functions and be detected/selected in survey data. In Section 8 we discuss how various properties affect the Lyα output, and under what conditions galaxies may emit their Lyα. Finally in Section 9 we present a summary of our findings. Throughout we assume a cosmology of $(H_0, \Omega_M, \Omega_\Lambda) = (70\ \mathrm{km\ s^{-1}\ Mpc^{-1}}, 0.3, 0.7)$.

2. OVERVIEW OF THE DATA

A detailed description of the data and its reduction, binning, and processing can be found in Paper I, and here we present only a brief overview. All 14 galaxies were imaged with *HST* in three filters that isolate the emission lines: optical narrowband filters for Hα and Hβ with either the WFC3 or ACS, and a UV long-pass pair-subtraction method to isolate a clean well-defined intermediate bandpass that captures Lyα using the Solar Blind Channel (SBC) of ACS (see Paper I and Hayes et al. 2009). Further to this we obtained FUV continuum imaging (SBC) and optical broadband imaging in approximately the *U*-, *B*-, and *I*-bands (ACS and/or WFC3); exactly which filter depends on redshift (Paper I). Imaging data were reduced with their standard *HST* `CALACS` and `CALWF3` pipelines, and drizzled onto a common pixel scale of 0.″04 using the `MULTIDRIZZLE` task (Fruchter & Sosey 2009). Finally reduced images were matched in point-spread function (PSF) using the image with the broadest PSF as reference. ACS/SBC photometric zero-points were corrected following the method described in Paper I.

Science frames were adaptively binned using a Voronoi tessellation algorithm and the weight maps output from `MULTIDRIZZLE`. In this article we present results derived from both binned and un-binned frames, depending on the application. For this we used the Weighted Voronoi Tessellation (WVT) binning algorithm by Diehl & Statler (2006), which is a generalization of the Voronoi binning algorithm of Cappellari & Copin (2003). For the reference bandpass we use the FUV continuum image and require a threshold signal-to-noise ratio of 10 per bin, but do not permit bin sizes to exceed 1 arcsec^2 (625 pixels at the native scale of WFC3/UVIS).

The Lyα-transmitting UV filter was continuum-subtracted using the *Lyman-alpha eXtraction Software* (`LaXs`), which is an extension of the method presented in Hayes et al. (2009), where full control of the nebular spectrum is obtained through narrowband imaging in Hα and Hβ. `LaXs` also handles the iterative continuum subtraction of Hα and Hβ, and estimates the stellar absorption under Lyα (see Valls-Gabaud 1993) and each Balmer line (e.g., González Delgado et al. 1999). The continuum subtraction of Hα is also corrected for the contribution of both [N II] $\lambda\lambda$6548, 6584 lines at the appropriate transmission level, where the [N II]/Hα ratio (*N*2 index) is measured in the Sloan Digital Sky Survey (SDSS) spectrum. Thus it accounts for no spatial variation, although this effect is shown not to be strong in most local starbursts.

We caution again that, because Lyman series transitions occur to the ground-state, interstellar H I absorption in the Lyα resonance can be very strong. This absorption affects not only nebular Lyα, but also $\lambda = 1216$ Å radiation in the stellar continuum which, particularly along sightlines to the brightest clusters, can be substantial. Furthermore, the associated scattering and frequency redistribution of these photons may result in complicated, extended, and P-Cygni-like

line profiles (e.g., Mas-Hesse et al. 2003), the absorption components of which may extend hundreds of km s^{-1} blueward of line center. Imaging methods have no capability to correct for interstellar absorption nor disentangle the red and blue components of a P Cygni profile. What we refer to as Lyα in this paper is any deviation from the predicted stellar UV continuum, integrated over the synthetic narrow bandpass. However we note also that if this constitutes a "problem" it is not one that is unique to low-z observations, as high-z narrowband imaging (and also low-resolution spectroscopy) will see the same blend of absorption and emission. Indeed the high spatial resolution afforded by *HST* imaging at low-z enables us to see precisely where emission and absorption dominate in the ISM, and simulations of LARS galaxies observations at the degraded spatial sampling of higher redshifts are ongoing (L. Guaita et al., in preparation).

The output of `LaXs` includes not only emission line and line-free continuum images, but also maps of the stellar age and mass, and attenuation seen by the stellar continuum; several of these additional outputs are also used for analysis in this paper.

3. IMAGES AND LINE MAPS

3.1. Line Intensity Maps

We present our first results in Figure 1. Interloping objects, such as a field star in the frame of LARS 09 and a chance projection of a nearby galaxy in the frame of LARS 11, have been masked in these frames. The far left column shows the observed intensity of radiation in the FUV, which traces the unobscured massive stars, and roughly incorporates the sites that produce the ionizing photons (LyC). In the center left column we show continuum-subtracted Hα, which traces the nebulae in which the aforementioned ionizing photons are absorbed. Morphologically the FUV and Hα emission maps are very similar, which is to be expected if LyC photons do not travel great distances; the flux emitted at one wavelength roughly results from the other. Discrepancies between FUV continuum and Hα may result from dust attenuation (which would obscure the UV more than Hα, at least for the approximation of a dust screen), an evolved stellar population (e.g., an A-star dominated region will not produce ionizing photons, but will remain bright in the FUV), or the fact that we can spatially resolve the nebulae from their ionizing sources. Some galaxies, for example LARS 03 and 05, do show somewhat extended Hα, whereas in others such as LARS 01 and 06, Hα appears more compact. While we have not yet dust-corrected the Hα frame, its unobscured intensity traces the underlying production of Lyα. The continuum-subtracted Lyα observation is shown in the center right panel, and in the far right column with UV contours. Immediately it can be seen that these Lyα morphologies bear only limited resemblance to their counterparts in the FUV and Hα: in some cases Lyα appears to be almost completely absent, whereas in others smooth, large-scale structures are visible that are not seen at other wavelengths (see also Hayes et al. 2013).

The intensity scaling of all the images is logarithmic, and the cut levels are set to show the maximum of structure and the level at which the faintest features fade into the background noise. Should the reader wish to compare galaxies in absolute surface intensity, they are referred to Section 4 and Figure 3. Lyα can appear in absorption as well as emission but these logarithmic images do not display any relative information of Lyα intensity below zero. Despite this tuning to show detail in emission, some galaxies are almost invisible in Lyα: LARS 04 and 06 in particular show only small hints of weak patchy Lyα emission but otherwise little sign of contiguous emission regions. We note that every galaxy in the sample shows *some* Lyα emission, although that does not necessarily qualify every galaxy as a "Lyα emitter" in the common sense of the term. Section 7 is dedicated to the discussion of this.

A general trend is that while the FUV and Hα images show a great deal of central structure, not much of that structure remains in the Lyα morphology. Many of the complexes of star-forming knots shown in Hα give way to much smoother and featureless Lyα images; LARS 05 and 08 are some particularly striking examples of this. The extended halo emission discussed in Hayes et al. (2013) is clearly visible, particularly in LARS 01, 02, 05, 07, 10, 12, 14.

ACS/SBC, through which our FUV images are obtained, is known to have a dark current that is centrally peaked, causing a pattern in the image that may be somewhat resemblant of our low surface brightness Lyα structures. However, we are convinced that none of the observed diffuse component is the result of this instrumental signature. First, and as discussed in Paper I, the SBC dark current increases as a strong function of operating temperature, which in turn grows with the time since the SBC amplifiers have been powered on—the dark current is constant and negligible at temperature below 28°C, which corresponds to about 4 hr of operation (Gonzaga et al. 2011). Our SBC observations were executed in visits of just two orbits, which corresponds to no more than 3 hr of operation. Furthermore we have been careful to make sure that our SBC visits are only executed when the camera has not been used in the preceding visits and the amplifiers have been switched off, thereby ensuring a cold detector when the observations begin. Secondly, we adopted a strategy of interleaving on- and off-line observations, such that a dark current signature should it somehow be present, would be evenly distributed between the filters. Finally, the fact that the extended halo feature is absent in 7 of the 14 galaxies (LARS 03, 04, 06, 08, 09, 11, 13), and that galaxies show differing morphologies, asymmetries, and intensities in the diffuse component all lead us to confidence about its reality.

3.2. Line Ratio Maps

In Figure 2 we show maps of the following ratios: Hα/Hβ, which quantifies the dust attenuation in the nebular phase (left); Lyα/FUV continuum, the EW ($W_{\mathrm{Ly}\alpha}$, center); and Lyα/Hα (right). Pixel-to-pixel noise in some of these images may be high, and usually comes from low signal in either the Lyα or Hβ image. To remove this from the presented images we restrict our display to the isophotal level in the UV that corresponds to twice the Petrosian radius, defined by $\eta = 0.2$ (Petrosian 1976). This is the isophotal version of the circular apertures used to compute the global quantities in Section 5.

Galaxies show varying degrees of structure in all the intensity ratios. In Hα/Hβ some objects (e.g., LARS 03) show smooth spatial gradients in their extinction, while others show very little well-defined structure (e.g., LARS 02). Spatially Hα/Hβ ranges between values as low as ~2 (notably in LARS 02), to galaxies that show heavily extinguished nuclei with Hα/Hβ above 8 (LARS 03 and 08). The Lyα EW, and Lyα/Hα maps are rich with features that reflect the complex Lyα astrophysics. The Lyα EW, shown in the central panels in Figure 2, is one of the most common high-z observables, and the main selection criterion for most Lyα surveys. At high-z, of course, the EW is always measured in collapsed apertures. For the color-scaling in

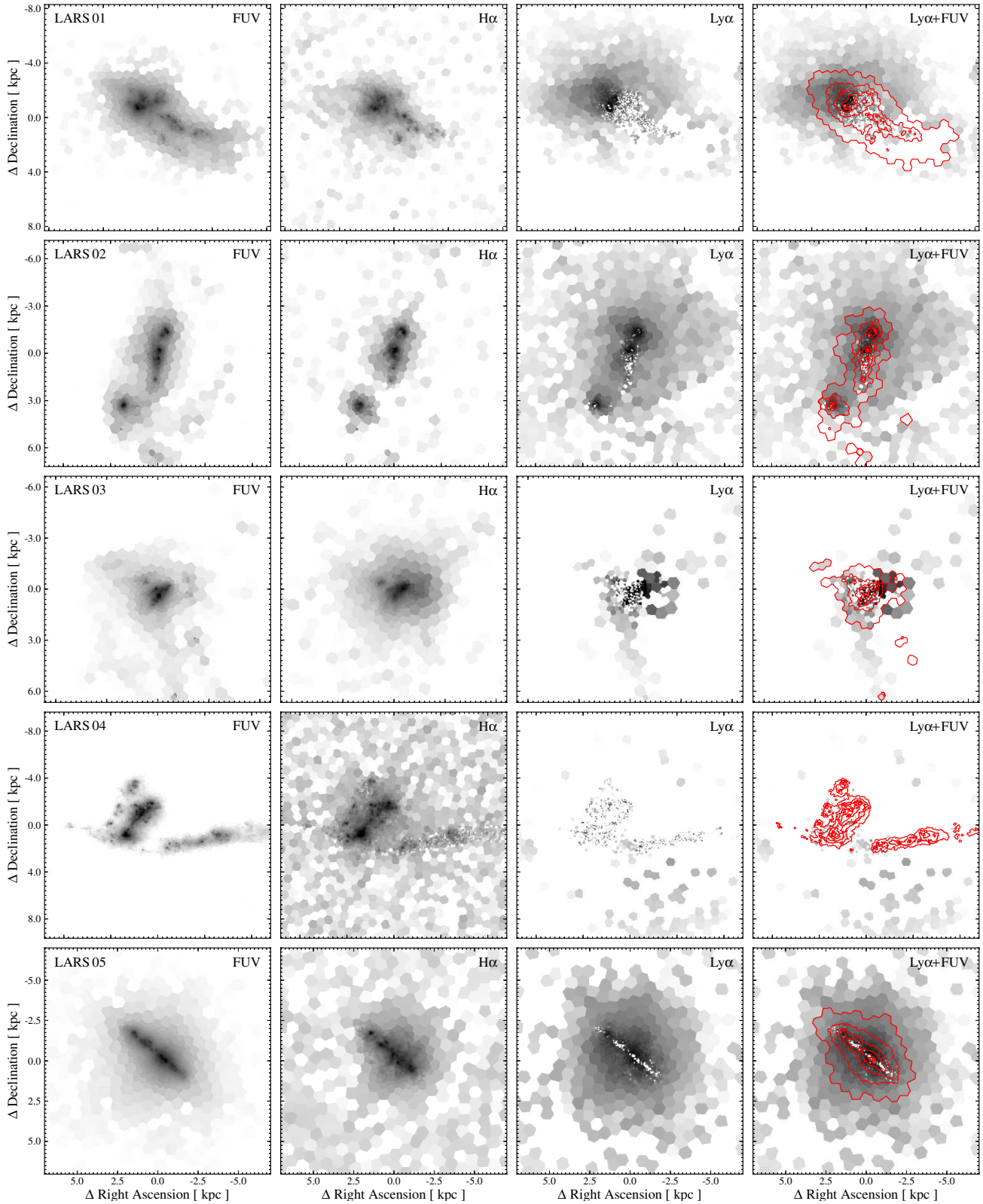

Figure 1. *HST* imaging of the LARS galaxies. Leftmost panels show the FUV continuum at $\lambda \approx 1500$ Å, which traces massive star-forming regions that are not obscured by dust. Center left panels show continuum-subtracted Hα, which traces the nebulae that result from star formation. The center right panels show continuum-subtracted Lyα maps, and the right most images are the same but with FUV contours overlaid in red. All images have been adaptively binned using Voronoi tessellation, and are shown in a negative logarithmic intensity scaling in which the cut levels are set to show detail. Lyα frames are continuum-subtracted, and hence these frames in particular can contain negative flux; in logarithmic scaling this is undefined so Lyα absorption along the line-of-sight is often seen as white speckles. Each cutout is scaled to show the overall galaxy morphology, so each object is shown on its own physical scale; the size in kiloparsecs is labeled for each object. North is up and east to the left. From top to bottom, galaxies LARS 01–14 are shown. In LARS 09 a field star has been masked with a square box and in LARS 11 a nearby projected spiral galaxy has been masked with the triangular shape.

(A color version of this figure is available in the online journal.)

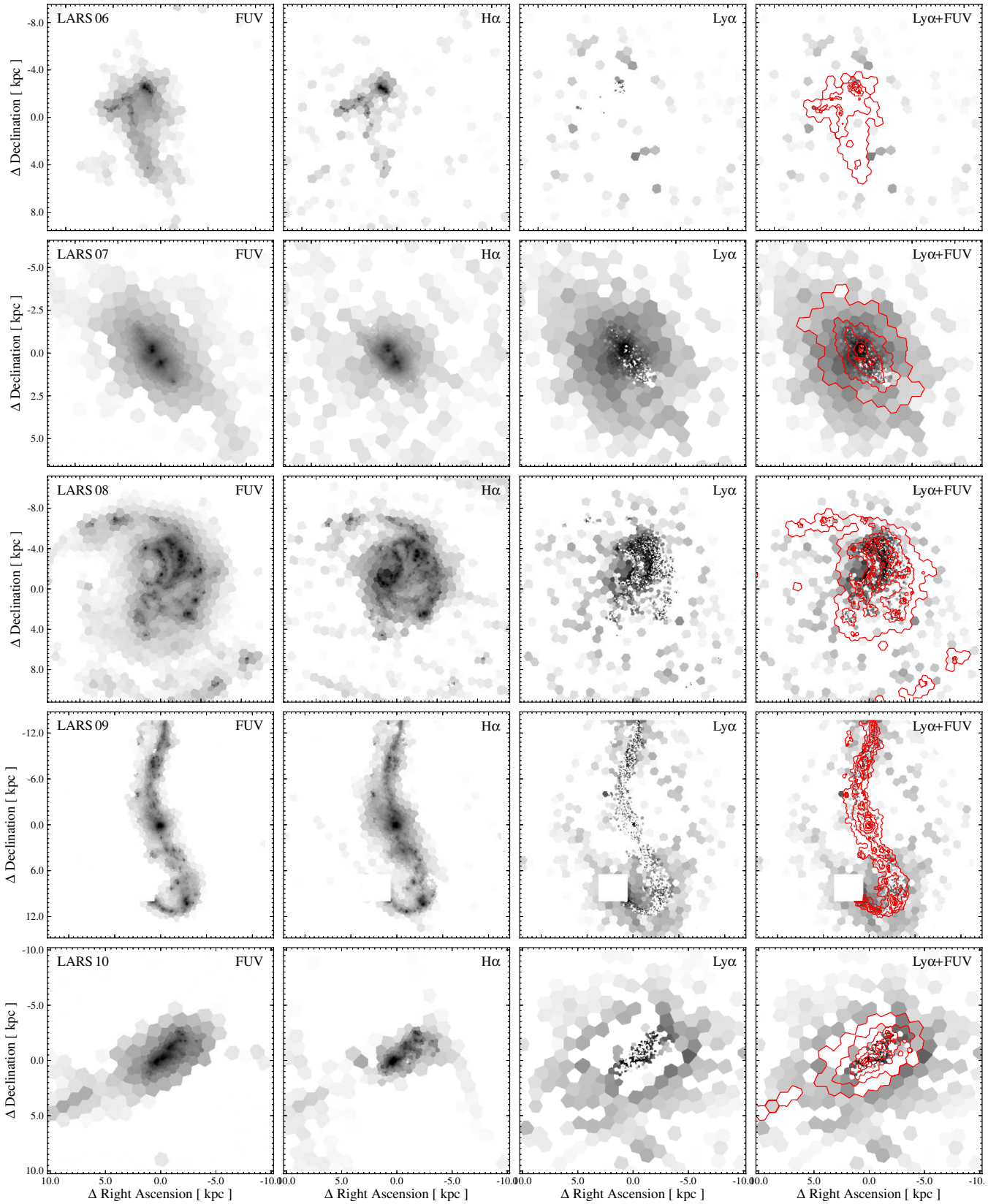

Figure 1. (Continued)

Figure 2, black shows an absence of Lyα (or absorption), a blue color encodes a Lyα EW of 100 Å, corresponding to the expected Lyα EW of star formation at equilibrium, and mid-green (250 Å) to the approximate value that can be attained for very young star formation episodes (Charlot & Fall 1993). All yellow, red, and white bins exceed this value. For the Lyα/Hα maps, the intrinsic ratio for case B recombination is 8.7 ($\approx$11 for case A; Hummer & Storey 1987). In the central regions of all galaxies,

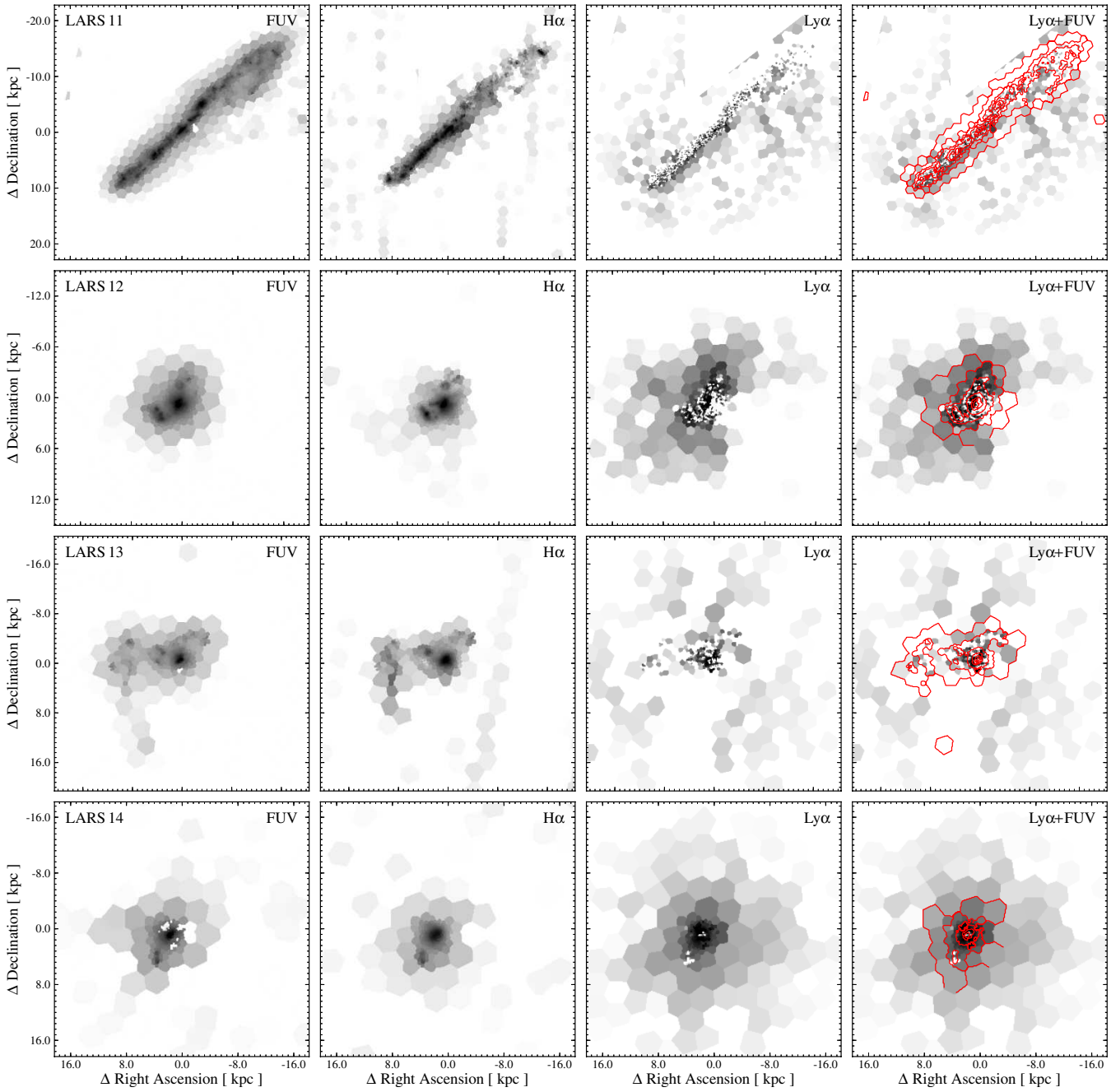

Figure 1. (Continued)

where the UV surface brightness is high, the overwhelming majority of the displayed pixels are in the black–purple range, showing EW below a few tens of angstroms, and Lyα/Hα in the range of <0 to $\sim$3. The low EWs can be explained if the star formation episode is in the process of turning off, but the Lyα/Hα ratio cannot: the black–purple pixels in the Lyα/Hα map can only be explained by a stronger suppression of Lyα than Hα. This could be because of dust attenuation or because Lyα photons are being resonantly scattered out of the line-of-sight by neutral hydrogen atoms. In many cases, however, the values of Hα/Hβ in these regions imply nebular attenuations of around zero, which would suggest that scattering is the dominant mechanism of removing photons from the sightline.

Another feature seen in most of the galaxies is that as we look away from the highest surface brightness regions, both the Lyα EW and Lyα/Hα ratios increase. In examples like LARS 05, a thin column of low ratios runs across the body of the galaxy, but rapidly increases away from the plane. In this example the EW exceeds 500 Å (twice the maximum value for a zero-aged star formation episode), and Lyα/Hα exceeds 30. One may certainly expect EWs to be high on small scales simply because the stars and the nebulae can be spatially resolved, but this cannot explain the high local line ratios. In Otí-Floranes et al. (2012) we showed that we could not easily produce such line ratios in collisionally excited plasmas, and these local enhancements must result from the scattering of Lyα into the line-of-sight.

One natural consequence of the larger EW at larger radius is that the integrated EW measured by matched aperture on-line/off-line photometry—as done for instance by SExtractor (Bertin & Arnouts 1996) in dual-image mode—will be strongly dependent upon the size of the aperture (see Section 5).

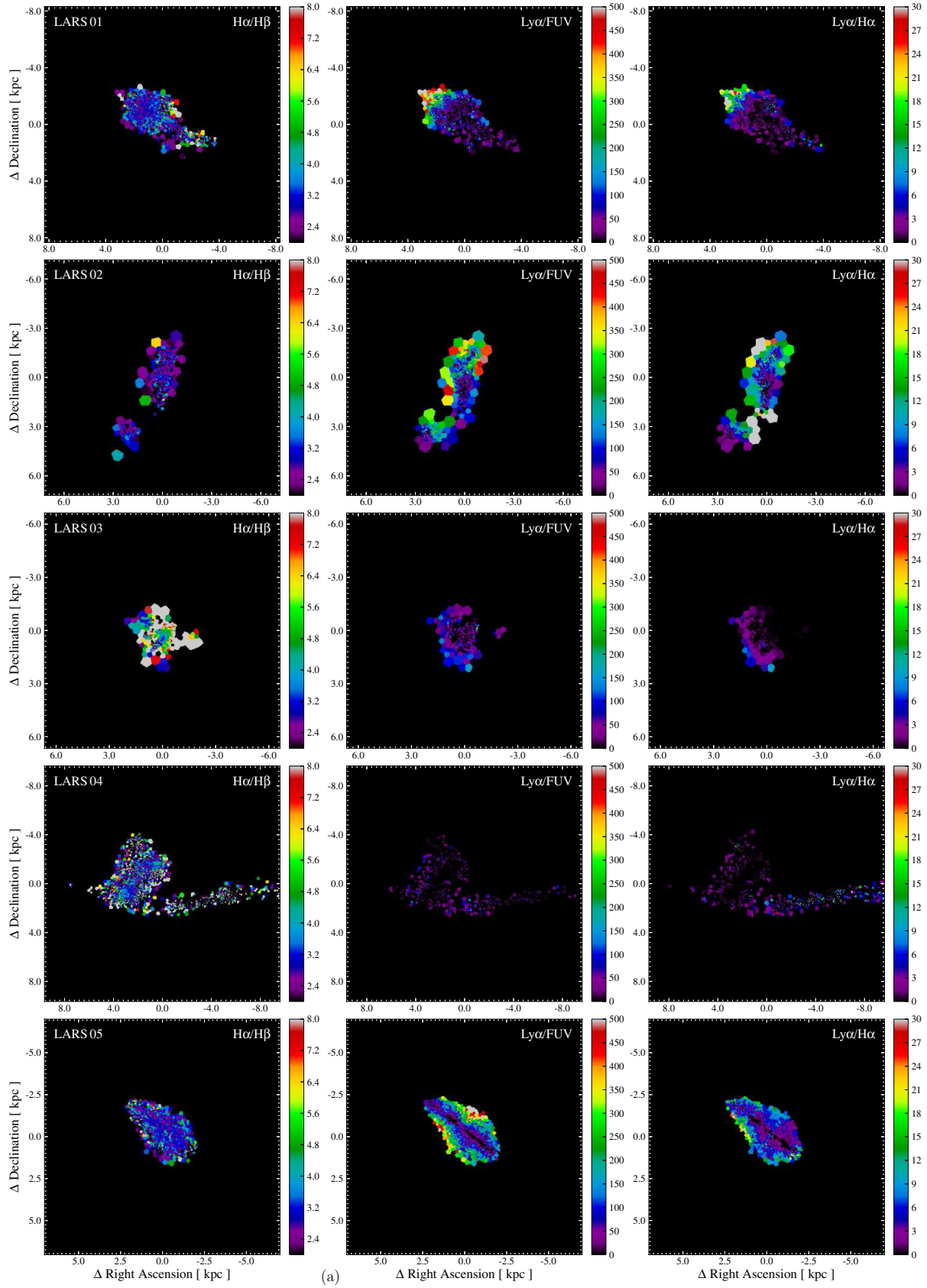

Figure 2. Line ratios for LARS (a) galaxies 01, 02, 03, 04, and 05. Left panels show Hα/Hβ, which approximates the attenuation due to dust in the nebular phase. For reference, note that Hα/Hβ for 10^4 K gas is 2.86 (Osterbrock 1989). Center panels show the Lyα EW—this takes a value of ≈100 Å for star formation at equilibrium (after roughly 100 Myr) and up to ≈250 Å for the youngest bursts (Schaerer 2003). The right panels show the Lyα/Hα ratios, which at normal temperatures and densities takes a value of ≈8.7 (Hummer & Storey 1987). Scales are the same as in Figure 1. (b) Galaxies: LARS 06, 07, 08, 09, and 10. Note that a star has been masked in the image of LARS 09. (c) Galaxies: LARS 11, 12, 13, and 14. Note that a galaxy has been masked in the image of LARS 11.

(A color version of this figure is available in the online journal.)

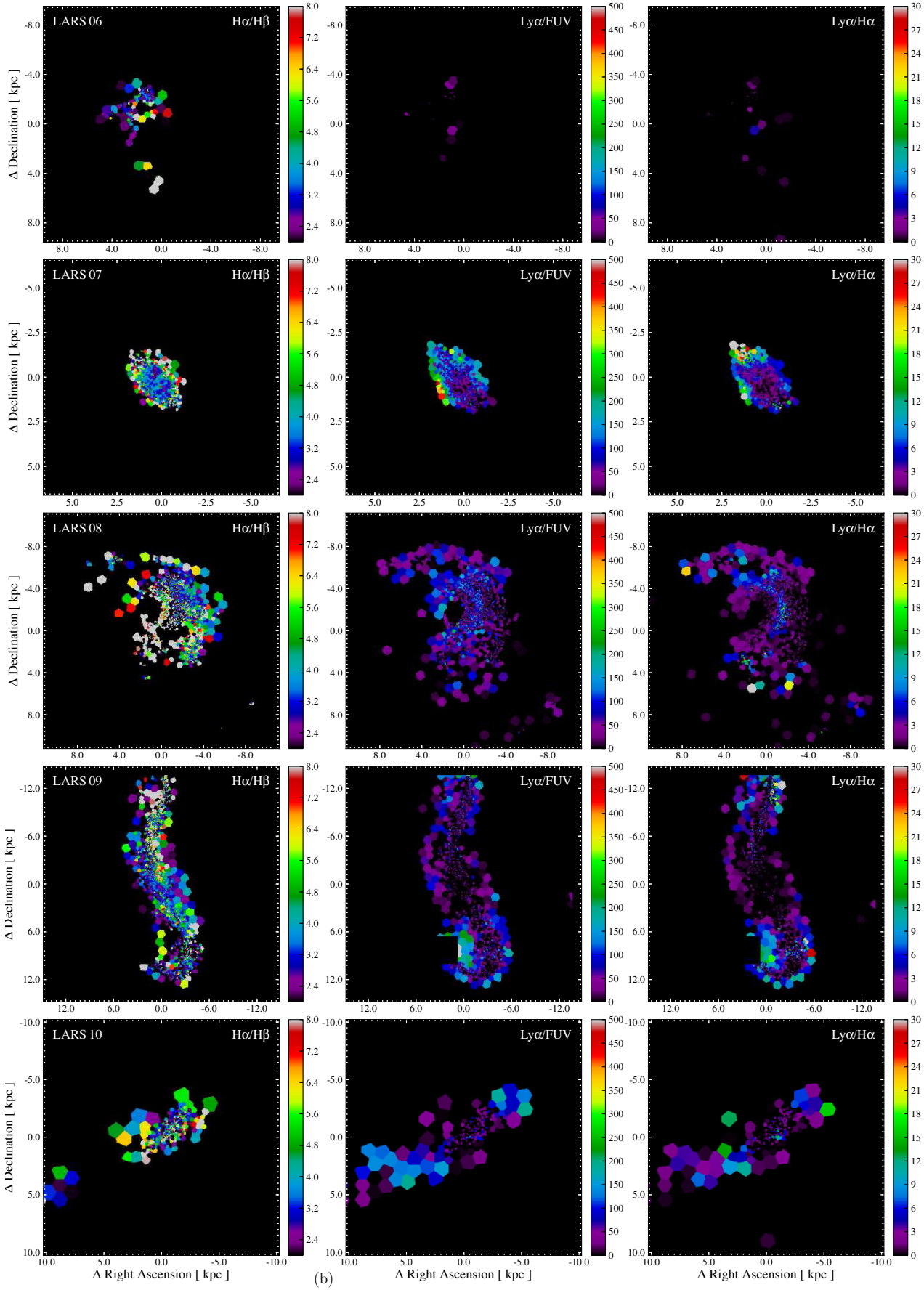

(b)

Figure 2. (Continued)

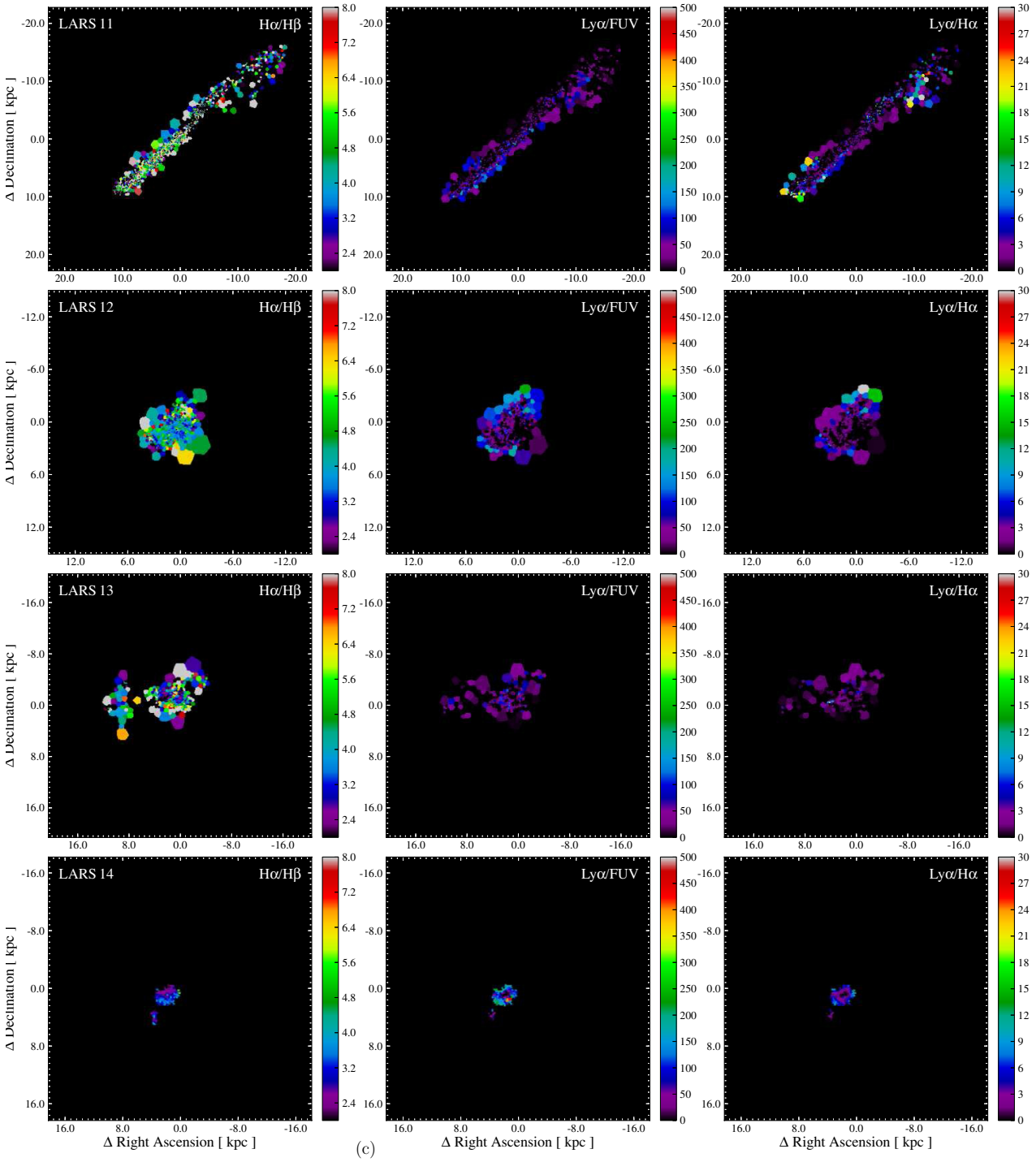

Figure 2. (Continued)

4. THE SPATIAL DISTRIBUTION OF LIGHT

We now quantitatively examine and compare the spatial distribution of quantities. In a high-z narrowband survey all galaxies will lie at effectively the same redshift, so the whole sample will have the same physical sampling scale and luminosity distance. This is not true for the LARS sample, where redshifts differ by a factor of six (0.028–0.18). Hence to compare galaxies equally we present all quantities in rest-frame luminosities (instead of flux) and converted onto the physical scale in kiloparsecs (instead of the observed angular scale in arcseconds)—i.e., when we refer to line "surface brightness," the units are erg s^{-1} kpc^{-2} (instead of erg s^{-1} cm^{-2} arcsec^{-2}). For reference a galaxy at $z = 3$ with an observed surface brightness of 10^{-18} erg s^{-1} cm^{-2} arcsec^{-2} would have an intrinsic rest-frame brightness of 1.30×10^{39} erg s^{-1} kpc^{-2} for our assumed cosmology.

The galaxies have various morphologies and the inclinations of the underlying starburst hosts are currently unknown. Hence for radial work we attempt no deprojection and use simple

circular annuli; when we have obtained deep optical/NIR imaging for the sample we will study radial profiles and inclinations in more detail.

We describe the light distribution in two ways: firstly we present the radial profiles of quantities measured locally within annular apertures (Section 4.1), which describes how the emergent light is actually distributed as a function of radius, and is common in detailed spatial studies of low-z galaxies. Secondly, we show the summed quantity within each aperture (same as above) in Section 4.2. This is more comparable to the integrated measurements that would be made at high-z. In determining the center we simply adopt the brightest pixel in the UV continuum image. This is the same as in Hayes et al. (2013) and, while it is possible to make the case for other centroids, is the same as will be used for isophotal light profiles used in forthcoming studies.

4.1. Radial Profiles

Figure 3 shows the radial distribution profiles of Lyα an the FUV continuum, which are presented logarithmically to simultaneously contrast low and high surface intensities. The cost is that regions where Lyα is on average absorbed cannot be visualized. Typically the profiles are more strongly peaked toward the center in the continuum than in Lyα: in the inner regions Lyα profiles run systematically flatter than their FUV counterparts. To quantify this central peaking, we fit Sérsic light profiles[15] to both line and continuum, finding the profiles adequately approximate reality in most cases. Recovered indices, n, are found to be high in the continuum—usually between 4 and 8—which are typical of the very compact nature of the UV. Lyα profiles, however, typically show indices around $n = 1$–2, and much closer to the exponential profile seen in disk galaxies.

In the right panels of Figure 3 we present radial profiles of the Lyα/Hα ratio in the same annuli. Values of Lyα/H$\alpha > 8.7$ are shaded gray to indicate where the intrinsic value of the line ratio is exceeded, and it is clear that this happens at some radius in most galaxies in the sample. Most notably LARS 01, 02, 05, 07, 08, and 14 show Lyα to greatly exceed the intensity that is predicted by the Hα line, and ratios three times the intrinsic value are easily obtained in some galaxies.

4.2. Photometric Curves-of-growth

In Figure 4 we show the total aperture-integrated FUV luminosity, and Lyα luminosity, EW, and $f_{\rm esc}^{\rm Ly\alpha}$ as a function of aperture radius. The upper left panel shows the cumulative FUV luminosity; naturally, with a strong central peaking of this light profile (Figure 3), this quantity increases monotonically and rapidly within the central few kpc. For all galaxies except one (LARS 11) these growth curves have essentially flattened by radii of $\approx$10 kpc, and all the more nearby ones (LARS 01–07), flatten by substantially smaller radii still (3–5 kpc), suggesting that all the light has been captured by the aperture. Lyα growth curves, shown to the upper right behave somewhat similarly, and most of these have also flattened by $r \sim 10$ kpc. However some (LARS 08, 09, 11, 13 at least) show profiles that are still growing at radii corresponding to the full extent of the SBC detector. LARS 04 and 06 are strong Lyα absorbing galaxies, for which as radii become larger more Lyα flux is absorbed. Similar behavior is seen in LARS 09 at small radii, but at $r \gtrsim 4''$ positive Lyα flux starts to be captured, the curve increases, and LARS 09 becomes a global emitter by about 10 kpc.

[15] $\mu(r) = \mu_0 \exp[-(r/r_0)^{(1/n)}]$.

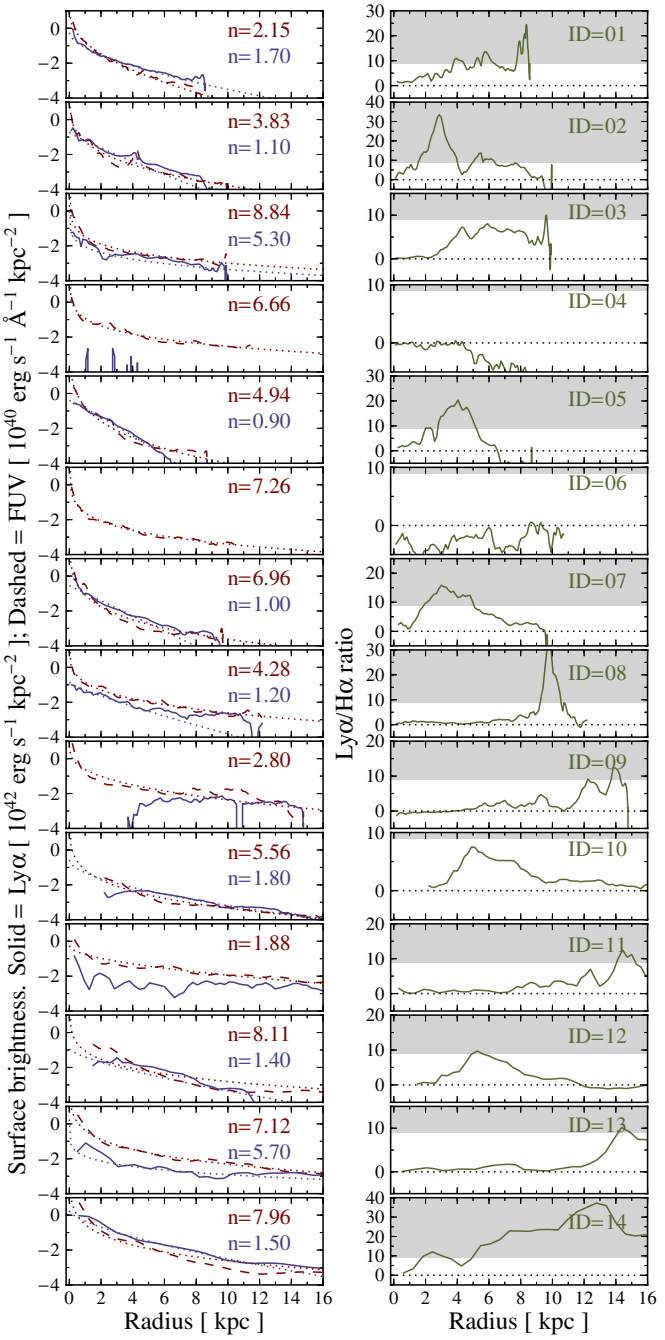

Figure 3. Left panels show the radial (circular annuli) light profiles computed from the Lyα (blue solid) and FUV (red dashed) images. For comparison, profiles are scaled from observed surface brightnesses to rest-frame emissivities per areal unit, and units of the ordinate axis are 10^{42} erg s^{-1} kpc^{-2} for Lyα and 10^{40} erg s^{-1} Å^{-1} kpc^{-2} the continuum. Best-fitting Sérsic profiles are shown with dotted lines of the corresponding colors, and the recovered Sérsic index, n, is listed for each. Right panels show the local Lyα/Hα ratios in the same annuli. The gray shading shows regions for which the intrinsic case B value for this line ratio is exceeded.

(A color version of this figure is available in the online journal.)

The lower left panel shows aperture growth of $W_{\rm Ly\alpha}$, or simply the ratio of the upper right and upper left plots. The positive gradient in nearly all of the lines shows that the UV light is more strongly centrally concentrated than Lyα (cf. Section 4.1 and Figure 3). Some of these curves converge at rather high $W_{\rm Ly\alpha}$, above 40 Å, and two galaxies show $W_{\rm Ly\alpha}$ around 100 Å. The gray shaded area shows $W_{\rm Ly\alpha}$ above 20 Å, the canonical

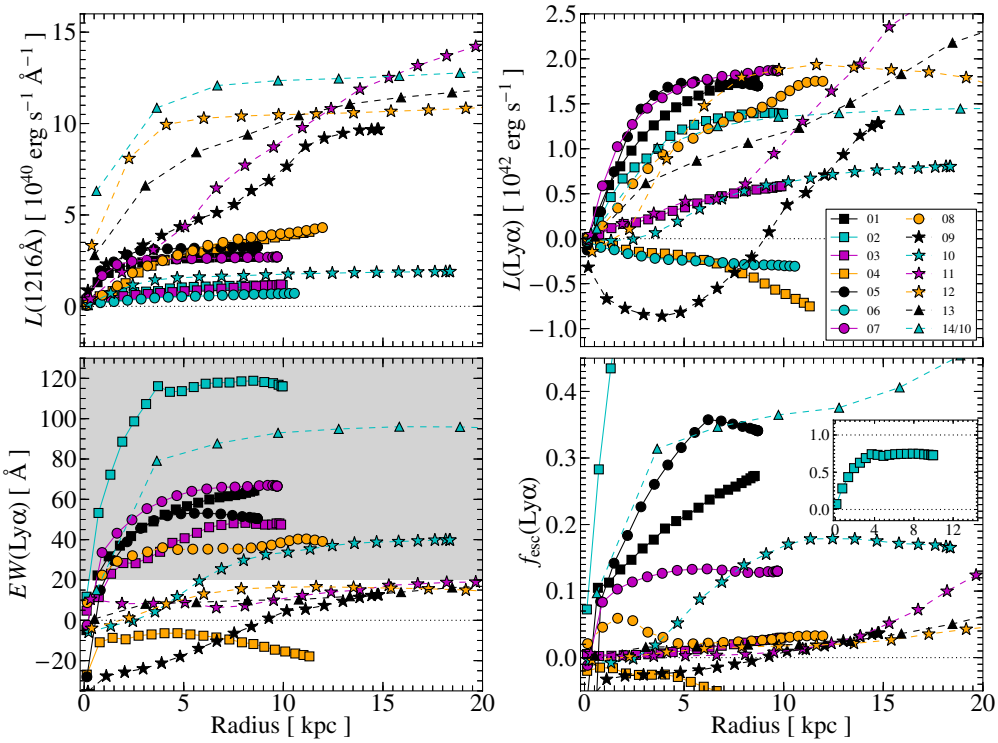

Figure 4. Radial photometric curves-of-growth. That is, the same as Figure 3 but instead of averaging over the differentially masked region, we integrate inside the total aperture. We show the FUV luminosity (upper left), Lyα luminosity (upper right), Lyα EW (lower left), $f_{\rm esc}^{\rm Ly\alpha}$ (lower right). In the plot of Lyα luminosity, the curve for LARS 14 has been divided by 10 so that the galaxy may be visualized. In the figure of $W_{\rm Ly\alpha}$, the shaded region shows $W_{\rm Ly\alpha} \geqslant 20$ Å, the common criterion used to select Lyα emitters at high redshift.

(A color version of this figure is available in the online journal.)

value by which Lyman alpha Emitters (LAEs) are defined at high-z, and we see that eight of our galaxies enter this region at some radius to which our *HST* observations are sensitive. However between radii of ≈10 and 20 kpc, the $W_{\rm Ly\alpha}$ of four galaxies is still slowly growing, reaching almost this threshold value by 20 kpc (≈2.″5 aperture at $z \gtrsim 2$). Whether they would become canonical LAEs using larger apertures we cannot say. As we will discuss in Section 7 these curves of $L_{\rm Ly\alpha}$ and $W_{\rm Ly\alpha}$ completely determine at what radius a high-z galaxy may be selected as an LAE.

The lower right panel shows the measured Lyα escape fraction, $f_{\rm esc}^{\rm Ly\alpha}$, which is defined here and throughout as the observed Lyα luminosity divided by the intrinsically produced luminosity. This value is derived from the Hα luminosity that has been corrected for nebular dust attenuation using Hα/Hβ and following Hayes et al. (2005):

$$f_{\rm esc}^{\rm Ly\alpha} = L_{\rm Ly\alpha}^{\rm obs}/L_{\rm Ly\alpha}^{\rm int} = L_{\rm Ly\alpha}^{\rm obs}/\left(8.7 \times L_{\rm H\alpha}^{\rm obs} \times 10^{0.4 \cdot E_{B-V} \cdot k_{6563}}\right). \quad (1)$$

E_{B-V} in this case is the nebular value derived from the ratio of Hα/Hβ, where we adopt the intrinsic ratio of 2.86 (Osterbrock 1989) and use the extinction curve derived in the Small Magellanic Cloud (SMC; Prevot et al. 1984). Qualitatively the picture does not change if we adopt other extinction laws. The way $f_{\rm esc}^{\rm Ly\alpha}$ has been defined permits it to take negative values in the case of Lyα-absorbing galaxies, and represents the additional fraction of continuum Lyα absorbed relative to the intrinsic nebular luminosity. We elect not to use global laws of effective attenuation such as that of Calzetti et al. (1994) or Charlot & Fall (2000) because the scales we probe are very different from those over which such laws were computed (tens of parsecs versus several kiloparsecs).

Generally most galaxies exhibit low escape fractions, below a few percent, while five objects show $f_{\rm esc}^{\rm Ly\alpha}$ above 10% (and growing) at the largest radii. The slopes of these curves differ markedly, with some rising sharply (e.g., LARS 02, 05, 14) and some much more slowly. Convergence also differs greatly: LARS 02 (inset) flattens at $f_{\rm esc}^{\rm Ly\alpha} \approx 75\%$ within ≈4 kpc, but in LARS 11 and the others with slowly rising $W_{\rm Ly\alpha}$, $f_{\rm esc}^{\rm Ly\alpha}$ continues to grow until radii of at least 20 kpc.

5. APERTURE-INTEGRATED PROPERTIES

Next we examine how total Lyα-related quantities compare with physical properties that can be derived from our *HST* imaging data, or survey data that have been previously obtained (SDSS spectroscopy). Properties derived from other data sets, e.g., H I masses and kinematics, will be presented in forthcoming articles. The results of Section 4 have already demonstrated that the computation of global Lyα quantities is a strong function of the adopted radius, but nevertheless it is illustrative to define a standard radius and compare the galaxies equally in terms of the derived quantities. For this we choose to adopt the frequently used definition of $2 \times r_{\rm P20}$, where $r_{\rm P20}$ is the isophotal Petrosian radius, determined to be the isophote at which the ratio of local to internal surface brightness, η, reaches 0.2. We calculate these apertures in the image that transmits Lyα and the FUV continuum, and use the same definitions as in Hayes et al. (2013) and L. Guaita et al. (in preparation).

We report a number of observable quantities of the emission lines and adjacent continuum in Table 1. Further

Table 1
Line and Continuum Properties of the LARS Galaxies

LARS ID	Common Name	z	$2 \times r_{P20}$ (kpc)	$L_{Ly\alpha}$ (10^{42} cgs)	L_{FUV} (10^{40} cgs)	$W_{Ly\alpha}$ (Å)	$L_{H\alpha}$ (10^{42} cgs)	$W_{H\alpha}$ (Å)	$L_{H\beta}$ (10^{42}cgs)	$W_{H\beta}$ (Å)
(1)	(2)	(3)	(4)	(5)	(6)	(7)	(8)	(9)	(10)	(11)
01	Mrk 259	0.028	2.39	0.85	2.52	33.0	0.63	409	0.11	73.9
02	···	0.030	2.32	0.81	0.96	81.7	0.18	313	0.08	69.4
03	Arp 238	0.031	1.87	0.10	0.57	16.3	0.59	199	0.14	26.8
04	···	0.033	1.83	0.00	3.02	0.00	0.60	242	0.20	44.4
05	Mrk 1486	0.034	1.88	1.11	3.00	35.9	0.51	436	0.17	66.7
06	KISSR 2019	0.034	1.30	0.00	0.53	0.00	0.08	166	0.04	41.2
07	IRAS 1313+2938	0.038	1.74	1.01	2.38	40.9	0.52	434	0.15	57.2
08	···	0.038	9.76	1.00	4.32	22.3	1.50	96.7	0.29	15.0
09	IRAS 0820+2816	0.047	10.1	0.33	9.47	3.31	2.61	247	0.62	40.5
10	Mrk 0061	0.057	5.28	0.16	1.70	8.90	0.34	85.1	0.08	14.9
11	···	0.084	16.0	1.20	15.0	7.38	1.66	65.3	0.29	10.7
12	SBS 0934+547	0.102	3.98	0.93	9.98	8.49	1.96	418	0.54	33.2
13	IRAS 0147+1254	0.147	7.94	0.72	10.4	6.06	2.46	195	0.63	26.0
14	···	0.181	1.62	4.46	9.60	39.4	1.99	947	0.94	120.

Notes. Redshifts (Column 3) are derived from SDSS. All quantities are computed within $2 \times r_{P20}$ light radii in the UV, which are given in Column 4. Equivalent widths are given in the rest frame. No quantities are corrected for extinction.

Table 2
Inferred Properties of LARS Galaxies

LARS ID	$E^{neb.}_{B-V}$ (mag)	$E^{stel.}_{B-V}$ (mag)	Age (Myr)	Mass ($10^9\,M_\odot$)	Lyα/Hα	Hα/Hβ	$f_{esc}^{Ly\alpha}$	$SFR^{H\alpha}$ ($M_\odot$ yr^{-1})	SFR^{FUV} ($M_\odot$ yr^{-1})	$SFR^{H\alpha}_{corr.}$ ($M_\odot$ yr^{-1})	$SFR^{FUV}_{corr.}$ ($M_\odot$ yr^{-1})
(1)	(2)	(3)	(4)	(5)	(6)	(7)	(8)	(9)	(10)	(11)	(12)
01	0.112	0.019	7.14	6.10	1.36	3.20	0.119	4.97	2.48	6.52	3.14
02	0.000	0.005	7.95	2.35	4.53	2.77	0.521	1.41	0.95	1.41	1.01
03	0.717	0.115	23.4	20.1	0.16	5.85	0.003	4.65	0.56	26.3	2.41
04	0.106	0.010	13.5	12.9	0.00	3.18	0.000	4.74	2.97	6.13	3.37
05	0.148	0.007	4.71	4.27	2.16	3.32	0.174	4.06	2.94	5.81	3.23
06	0.000	0.013	10.5	2.09	0.00	2.50	0.000	0.61	0.52	0.61	0.62
07	0.336	0.009	7.78	4.75	1.94	4.00	0.100	4.12	2.34	9.27	2.61
08	0.469	0.058	40.4	93.3	0.67	4.57	0.025	11.8	4.24	36.8	8.81
09	0.281	0.038	11.3	51.0	0.13	3.79	0.007	20.6	9.30	40.7	15.0
10	0.302	0.025	39.7	21.5	0.47	3.87	0.026	2.69	1.67	5.59	2.29
11	0.348	0.033	25.6	121	0.72	4.05	0.036	13.1	14.7	30.5	22.3
12	0.759	0.024	7.44	7.41	0.48	6.10	0.009	15.5	9.80	97.0	13.3
13	0.497	0.048	7.19	59.2	0.29	4.70	0.010	19.5	10.2	64.8	18.8
14	0.187	0.012	3.21	1.75	2.24	3.45	0.163	15.8	9.43	24.8	11.0

Notes. Properties are derived inside the same apertures as those given in Table 1. Column 2: nebular E_{B-V} is estimated from Hα/Hβ assuming an intrinsic ratio of 2.86 for 10,000 K gas. Columns 3 and 4: stellar E_{B-V} and age are estimated from an SED fit to the stellar continuum. Column 5: mass refers to the stellar mass derived by resolved SED fitting. Columns 9–12: SFRs are calculated from the calibration of Kennicutt (1998) and are compiled for comparative purposes.

quantities derived from these line strengths and/or spectral energy distribution (SED) fitting (same apertures) are reported in Table 2. In images there are various ways of computing these integrated quantities. In this paper, fluxes, flux densities, and stellar masses are computed by simple summation, and wherever a ratio of two fluxes is presented the quantities are summed individually before dividing. Stellar attenuation and ages are computed from the two-dimensional (2D) images by taking a flux-weighted average (see below). We have also performed total photometry inside the same apertures in the *HST* images and run `LaXs` on these fluxes, verifying that results are very consistent. Quantities derived from the SDSS spectra can be found in Paper I.

Graphically we elect to compile a number of observable/derivable quantities of Lyα, that are frequently discussed. These include $L_{Ly\alpha}$, $W_{Ly\alpha}$, Lyα/Hα, and $f_{esc}^{Ly\alpha}$, which are presented in Figure 5 against *HST* aperture-derived quantities, and in Figure 6 against quantities derived from optical spectroscopy of the central regions. We compare with the following:

1. *Far UV continuum luminosity near Lyα, L_{FUV}.* L_{FUV} is derived from the modeled image of the stellar continuum in the filter that transmits Lyα (F125LP or F140LP). Thus it represents a very small extrapolation from the adjacent filter that samples the continuum alone (F140LP or F150LP). In the unobscured case, L_{FUV} traces the average SFR over the last few hundred megayears and for completeness we also compile the FUV SFR using the Kennicutt (1998) calibration, and correct this for dust using the attenuation measured on the stellar continuum. The FUV magnitude, or its corresponding SFR, are among the most frequently presented quantities in high-z studies.
2. *Instantaneous SFR, $SFR_{H\alpha}$.* This is derived from the dust-corrected Hα luminosity and adopting the calibration of Kennicutt (1998), which assumes a Salpeter initial mass function between limits of 0.1 and 100 $M_\odot$. The dust correction is done by adopting the E_{B-V} inferred from the Hα/Hβ ratio measured in the same apertures. The Hα luminosity is also corrected for [N II] $\lambda\lambda$6548, 6584

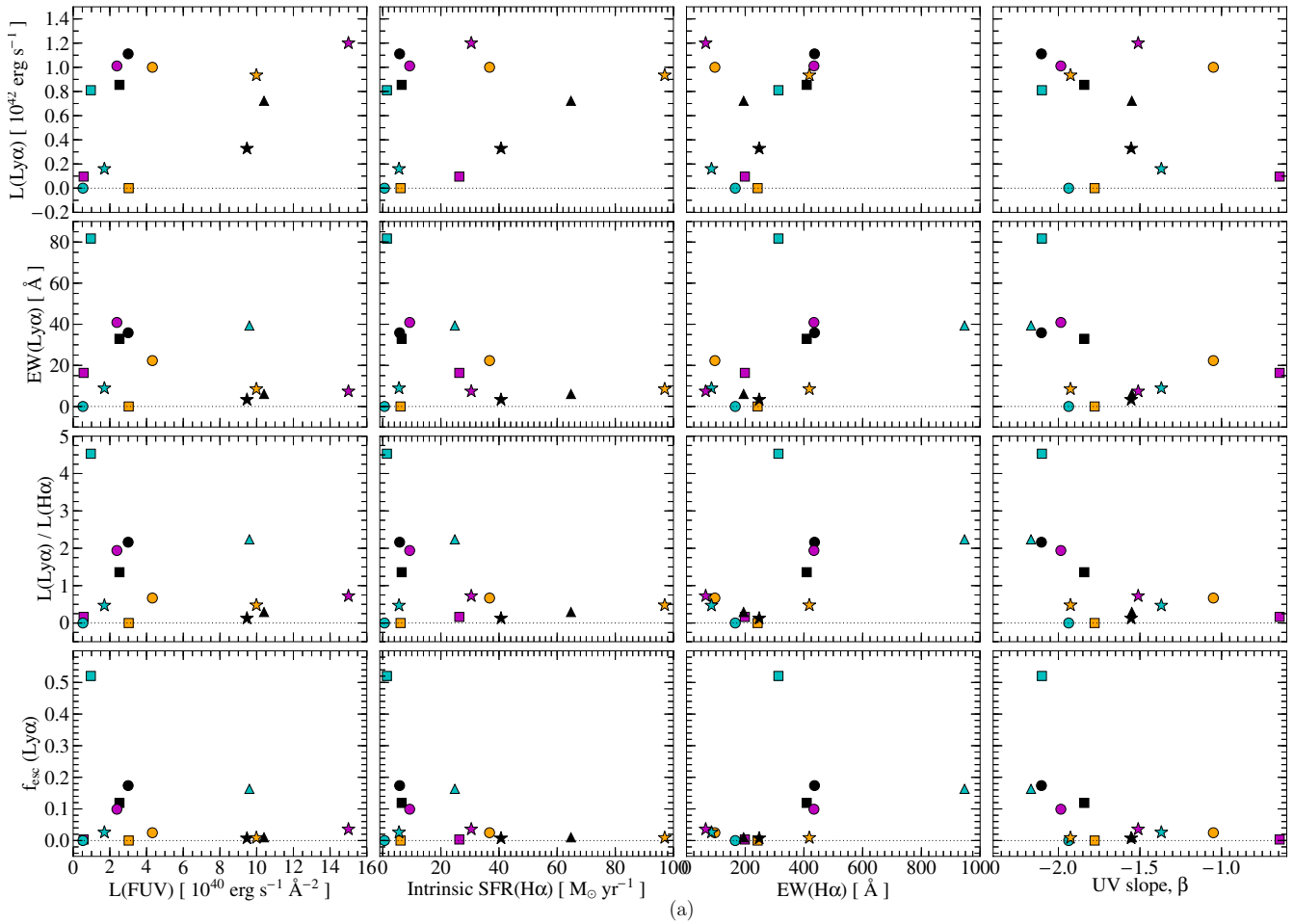

Figure 5. Comparison of "global" Lyα properties with quantities that can be derived from our *HST* imaging data. From top to bottom we show Lyα luminosity, rest-frame EW, Lyα/Hα, and $f_{\rm esc}^{\rm Ly\alpha}$ on the ordinate axis. These quantities have not been corrected for extinction. The upper plots of Lyα luminosity do not show LARS 14, which is four times more luminous than the next brightest system. From left to right we show (a) FUV luminosity, intrinsic (dust-corrected) instantaneous SFR derived from Hα and Hβ, Hα EW, and the UV continuum slope β. Symbols are the same as in Figure 4. (b) Nebular E_{B-V} derived from Hα/Hβ, stellar E_{B-V} derived from the SED fitting, the luminosity-weighted stellar age of the burst population derived also from the SED, and the total stellar mass (summed over underlying and starburst components).

(A color version of this figure is available in the online journal.)

emission (allowing for the filter transmission level) using the [N II]/Hα ratio measured in the SDSS spectrum, and also underlying Balmer absorption from stars (see Section 2).

3. *Hα equivalent width, $W_{\rm H\alpha}$.* This is computed by simply dividing the continuum-subtracted Hα flux by the total modeled continuum in the narrowband filter.
4. *Dust attenuation measured in the nebular gas, $E_{B-V}^{\rm neb}$.* This is estimated from Hα/Hβ, using the SMC extinction law (Prevot et al. 1984). Both lines have been corrected for underlying stellar absorption, Hα is corrected for [N II], and the quantity is fed back to the dust-correction of Hα and computation of $f_{\rm esc}^{\rm Ly\alpha}$ (above).
5. *Dust attenuation measured in the stellar population, $E_{B-V}^{\rm stel}$ from SED fitting.* This map is returned by the `LaXs` software on a pixel-by-pixel basis. For the computation of the global value we compute a flux-weighted average taking the *I*-band for the weighting bandpass: $\sum E_{B-V}^{\rm stel} L_I / \sum L_I$. Adopting other filters for weighting has negligible effect on our results.
6. *Age of the stellar population.* This is also output by `LaXs` as a 2D map, and the average is computed in the same way as for $E_{B-V}^{\rm stel}$.
7. *Mass of the stellar population.* This is also output by `LaXs` as a 2D map, and the sum is computed within the apertures.
8. *Nebular indices and metallicity, Z.* These properties are derived from the SDSS spectra. Because the SDSS fibers are of constant size (a standard 3″ diameter circle) and the defined *HST* apertures are variable, these apertures are not matched. Nonetheless each one is, or is derived from, a flux ratio, and they will provide a reasonable picture of the average oxygen abundance/excitation state in the galaxies and are at least consistent for every object. Because high-z observations of these rest-frame optical lines are becoming commonplace, at least around $z = 2$–3, we elect to show: the R_{23} index [≡ ([O II] 3727+[O III] 4959+[O III] 5007)/Hβ]; the $N2$ index [≡ log([N II] 6584/Hα)]; the excitation parameter, P [≡ ([O III] 4959, 5007)/([O II] 3727+[O III] 4959, 5007)]. For a standard strong-line metallicity, we

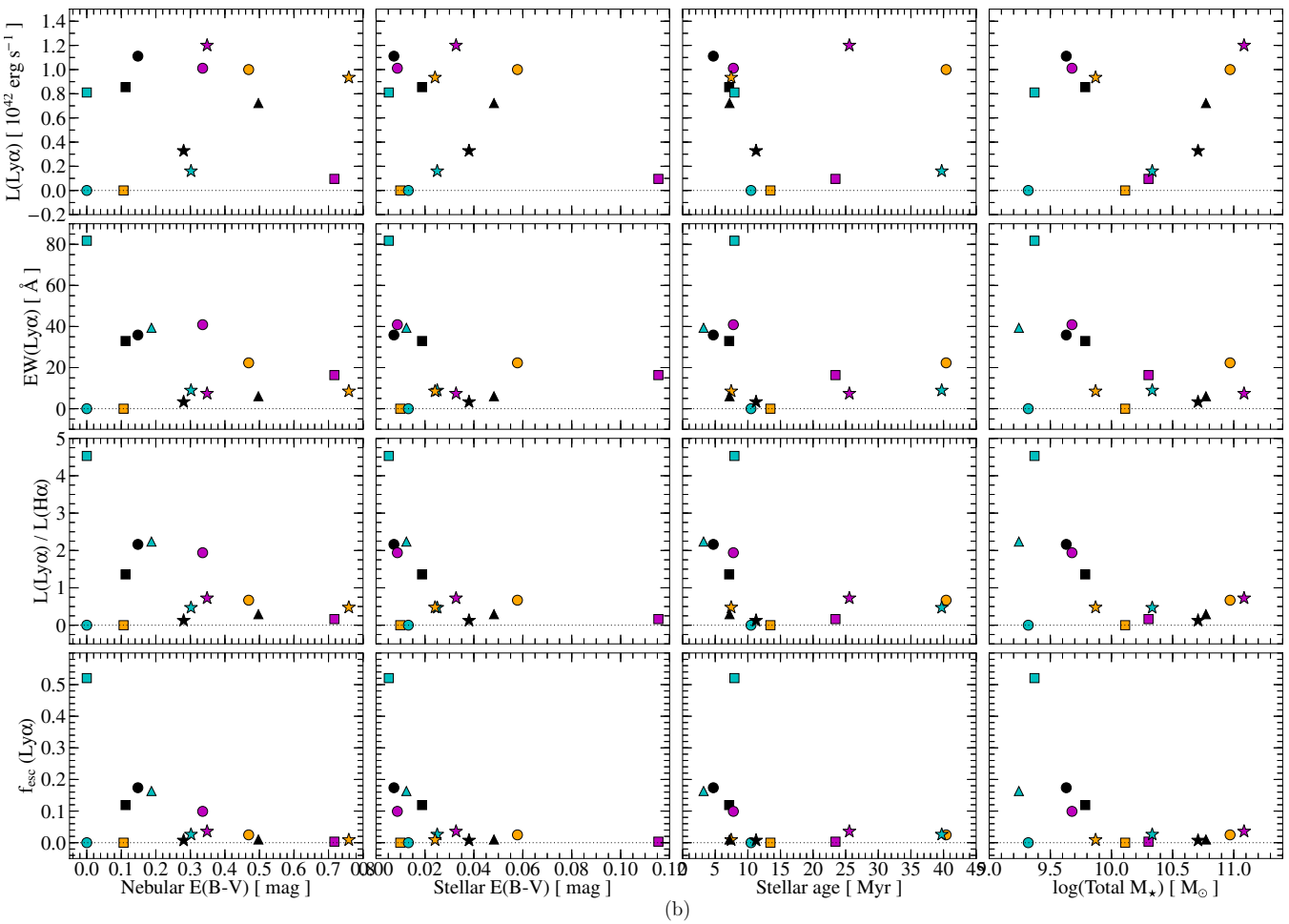

(b)

Figure 5. (Continued)

adopt the O3N2 method and the empirical calibration of Yin et al. (2007). For about half the sample we can make direct T_e-based estimates of the metallicity (Paper I) but as we cannot do so for the whole sample, we compare only strong line quantities, admitting the associated uncertainties.

The LARS sample comprises only 14 galaxies, and thus does not reach a high level of statistical significance. Nevertheless in sample size it is a three-fold improvement upon the existing body of work on low-z Lyα imaging (Östlin et al. 2009), and the sample is no longer biased by the selection of historically interesting "favorites" of the local starburst community. With global photometry in the UV and Lyα we are first able to compare our sample with high-z UV- and Lyα-selected samples, which we will do in Section 7. Furthermore with a larger number of galaxies than previously studied and many aperture-matched measurements, we may examine trends between Lyα output and various properties of the galaxies; this we do in Section 6. However, before discussing these results we will comment upon the individual galaxies.

6. COMMENTS UPON THE INDIVIDUAL TARGETS

LARS 01. LARS 01 (Markarian 259) is studied in detail in Paper I and also enters the sample of Wofford et al. (2013), so the reader is directed to these publications for more extensive information. It has a metallicity of $\approx$0.25 $Z_\odot$ (Paper I; Asplund et al. 2009), $\sim$0.1 mag of differential extinction (E_{B-V}) in the gas phase, has a modest SFR of a few $M_\odot$ yr^{-1}, and strong Hα emission with an EW of $\sim$400 Å. By these measures it is roughly comparable to ESO 338–IG04 (Hayes et al. 2005; Atek et al. 2008; Östlin et al. 2009). Indeed it is a strong Lyα-emitting galaxy: with an aperture EW of 35 Å and $>$50 Å globally, it would be likely selected as a high-z LAE; a luminosity of almost 10^{42} erg s^{-1} suggests that it could be detected by moderately deep surveys. Morphologically, it consists of a bright UV star-forming center, with an extended tail to the SW: there is a bright hot-spot of Lyα emission that emanates from the major star-forming condensation, and flows out in a diffuse fan-like structure preferentially in the NE direction. In this region the Lyα EW and Lyα/Hα ratio exceed 500 Å and 30, respectively. Such ratios would indicate substantial re-scattering of photons into the line-of-sight. Interestingly there is evidence for nebular filamentary structure in both Hα and Hβ that extends in this direction, which may indicate a bubble that expanded in this direction before blowing out. This would certainly be suggestive of a strong outflow of hot gas, which could also mitigate the trapping of Lyα photons and enable them to flow in this direction. The Lyα curves-of-growth, are all continually rising out to a radius of $\approx$8 kpc and $f_{\rm esc}^{\rm Ly\alpha}$ does not converge: it is likely that the total Lyα output from LARS 01 is somewhat higher than presented.

LARS 02. This galaxy shows a metallicity and Hα EW roughly similar to LARS 01, however with a SFR of around 1 $M_\odot$ yr^{-1} it is among the more dwarf-like objects in our

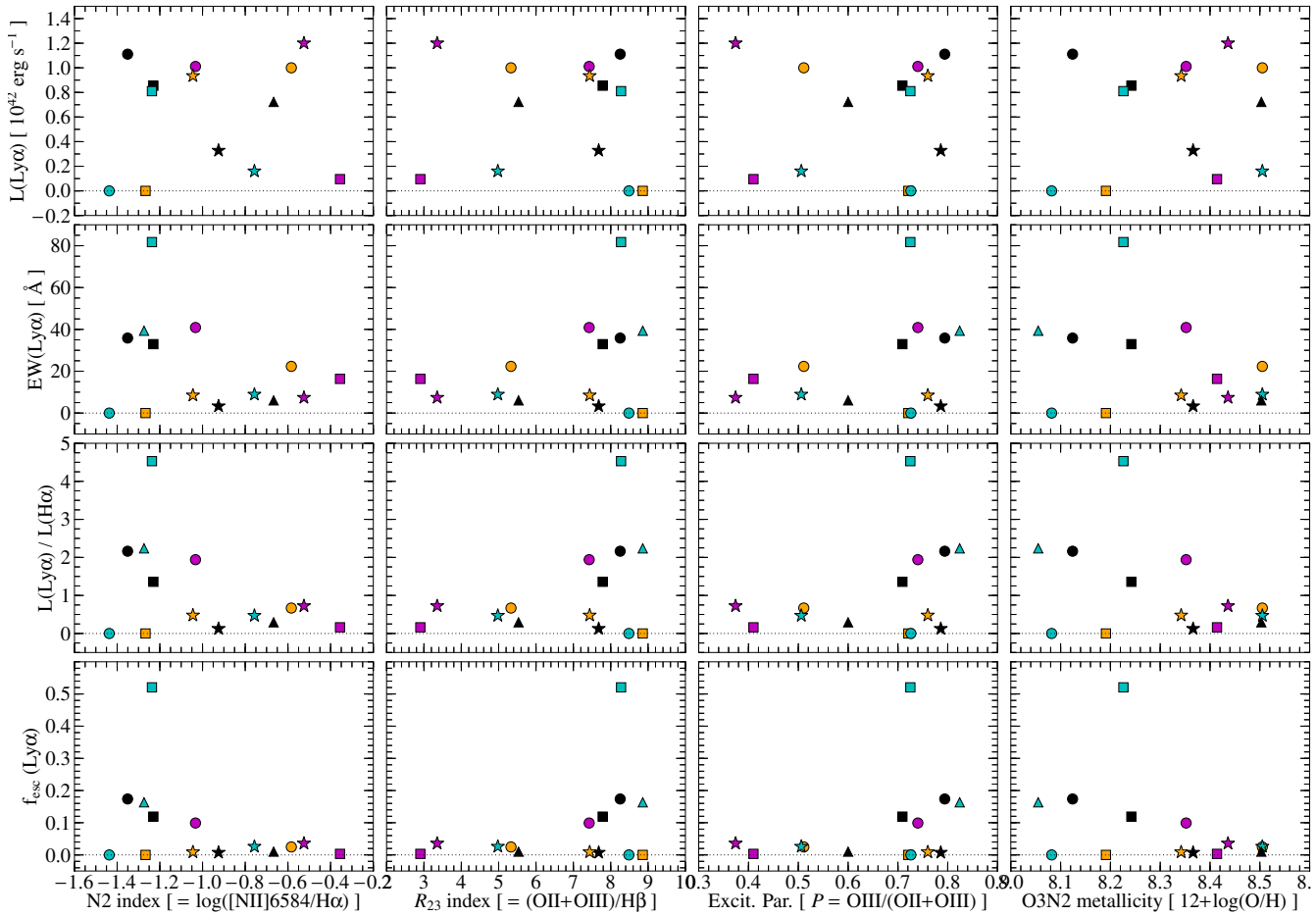

Figure 6. Same as Figure 5 but with properties derived from SDSS spectroscopy. As such these quantities have not been derived in the same apertures as those in which the Lyα quantities have been measured. From left to right we show: $N2$ index, R_{23} index, excitation parameter, and metallicity Z computed from the O3N2 index. Symbols are the same as in Figure 4.

(A color version of this figure is available in the online journal.)

sample. It is largely dust-free, and according to all the Lyα-related quantities is the strongest emitting LARS galaxy: Lyα EW almost 100 Å, Lyα/Hα = 4.5, $f_{\rm esc}^{\rm Ly\alpha} = 52\%$ inside the $2 \times r_{\rm P20}$ radius. Here again we see that the Lyα EW and Lyα/Hα ratio locally exceed their recombination values by large factors on kiloparsec scales, and the curves-of-growth for all the Lyα quantities rise very rapidly. Furthermore, this photometric curve-of-growth is rising so steeply that this galaxy emits 75% of its Lyα photons by a radius of 3.5 kpc. Such high levels of relative Lyα emission have not been observed before in targeted observations of local galaxies, although some Lyα-selected nearby galaxies have been seen to exhibit $f_{\rm esc}^{\rm Ly\alpha}$ higher than would be expected for their measured attenuations (Atek et al. 2009). It is plausible, although not required, that some mechanical enhancement of Lyα could produce such $f_{\rm esc}^{\rm Ly\alpha}$, or that we are either underestimating the intrinsic luminosity in Hα (or its dust correction by overestimating Hβ). Future X-ray observations could most likely provide the answer. LARS 02 would be selected as Lyα emitter in deep high-z surveys.

LARS 03. Arp 238 is among the most well-studied galaxies in the LARS sample. The galaxy comprises two merging nuclei and with ACS/SBC we were able to point at just one of the two cores. Our observation therefore covers only the southeastern nucleus. It is a luminous infrared galaxy and with a $\log(L_{\rm FIR}/L_{\odot}) = 11.8$ is close to the domain of ultra luminous infrared galaxies. Such IR luminous local galaxies have never before been imaged in Lyα; the most similar galaxy so far being NGC 6090 (Östlin et al. 2009), which is 0.4 dex fainter in $L_{\rm FIR}$. Arp 238 does show Lyα in emission with an EW of ~16 Å at twice $r_{\rm P20}$ and this rises to ≈40 Å when large apertures are considered. Thus it passes the canonical definition for high-z narrowband–broadband color selection. However the luminosity and escape fraction are small ($f_{\rm esc}^{\rm Ly\alpha} \approx 1\%$) and it is the simultaneous large extinction on the UV continuum that results in the high measured EW. This suggests that Lyα and the UV continuum are suppressed by roughly the same fraction. Within the spatial extents that we can probe with the SBC, the Lyα luminosity is low enough for LARS 03 to evade detection in all but the deepest high-z surveys, but the Lyα luminosity does continue to increase with radius out to 10 kpc; it is unclear what happens at larger radii.

LARS 04. LARS 04 shows a highly irregular UV morphology comprising an apparent bar and extended tail to the west. Lyα is emitted on small scales throughout all these regions, but in complete annuli a net absorption is found at all radii. Maps show that even on small scales the Lyα EW never exceeds expectations and no large-scale component of emission is apparent—between the UV-bright regions, where diffuse emission should easily be detectable, the continuum-subtracted Lyα flux negative, suggesting much neutral gas absorption is ongoing and if Lyα is emitted it must be on very large scales indeed. In terms of SFR and dust content it is quite similar to LARS 01, which emits copious Lyα.

LARS 05. Mrk 1486 is blue highly inclined (edge-on) disk galaxy with SFR of around $2\,M_{\odot}$ yr^{-1}. In the very central regions—along the plane of the disk—Lyα absorption of the stellar continuum is quite strong, and cancels much of the emission, resulting in a narrow absorbing band. However, this gives way to emission at small projected distances and Lyα luminosity and EW rise rapidly; EW $>$ 500 Å is reached at a projected distance of 2.5 kpc from the disk. The large-scale morphology is one of an azimuthally symmetric and featureless halo of emission, although the aperture growth curve in Lyα appears to flatten at a radius of 4 kpc, which would indicate that we are able to capture most of the Lyα emission. At brighter Lyα isophotes, however, the Lyα surface resembles more the shape of the UV disk where Hα filamentary structures that extend in the polar direction are visible. This is reminiscent of outflowing gas that has accelerated and become Rayleigh–Taylor (RT) unstable (Mac Low & McCray 1988; Cooper et al. 2008), and could explain the Lyα enhancement in the same directions by permitting radiation to stream in this direction before scattering in the halo, similar to the bubble to the NE of LARS 01. Inside the $2 \times r_{P20}$ radius (1.9 kpc) LARS 05 has a Lyα EW of 36 Å, and its total EW of ∼45 Å is reached by ≈4 kpc. By EW and luminosity LARS 05 would be selected in deeper surveys as a Lyα-emitting galaxy.

LARS 06. KISSR 2019 is the most feebly star-forming galaxy in the sample by both FUV and Hα measures, and also exhibits the lowest nebular metallicity ($12 + \log(O/H) = 8.08$; Paper I). It is effectively unreddened according to Hβ; the observation of which is of insufficient quality to trace the extinction over some of the outer of regions where we detect Hα. In the UV and Hα it reveals a morphology comprising one major star-forming condensation around which no hint of Lyα emission is seen. Most wavelengths also reveal a tail of stars extending to the south, although there is no evidence for this in Lyα either. Interestingly the tail is also rather weak in Hα, which suggests that the stars of which it is made up have evolved to the stage where they remain UV bright, but are not hot enough to produce strong nebular lines; this may be evidenced also by its age of ≈10 Myr. The galaxy shows strong Lyα absorption and an almost complete absence of emission over the surface.

LARS 07. Also known as IRAS 1313+2938 and KISSR 242, LARS 07 has already been studied in Lyα spectroscopically with *HST*/COS (France et al. 2010; Wofford et al. 2013). Morphologically LARS 07 resembles LARS 05 as an edge-on disk and is very compact in Hα and the stellar continuum. However there is evidence of some faint nebular gas extending away from the disk that is also somewhat extinguished as evidenced by Hα/Hβ. It also shows a large-scale and low surface brightness Lyα halo although this halo is somewhat extended in the direction of the disk. Like LARS 05 it also shows filamentary structure in Hα that extends away from the plane of the galaxy in the polar directions, again reminiscent of a RT unstable outflow. Very high local EW and Lyα/Hα are clear in these regions. In Lyα its growth curves follow those of LARS 01 and 05 closely and it seems that we have recovered almost all the Lyα photons at radii of 4 kpc. LARS 07 is among the more Lyα-luminous galaxies in the sample, and with an EW of ≈50 Å should be detected in most surveys.

LARS 08. This is a face-on disk-like galaxy with a heavily obscured nucleus, and shows the highest nebular metallicity in the sample according to strong-line diagnostics (Paper I). It shows numerous patches of UV-bright star-forming regions in the disk, that appears to be more extended to the west. Lyα emission is seen coming from the surface of this disk, but it is not strong compared to the FUV or Hα, with no significant super-recombination ratios visible at any position. Notably there is no sign of Lyα emission emanating from the nuclear regions, but instead Lyα is seen only from the regions that are brighter in the FUV, possibly as a correlation with the dust content. LARS 08 does show an ever increasing photometric curve-of-growth in its luminosity, but this does not translate into its EW or $f_{esc}^{Ly\alpha}$, which both flatten at smaller radii of about 2 kpc. This suggests that Lyα, FUV, and Hα all increase roughly similar ways with radius, at least for radii that we can probe. We caution also that this is one of the two most extended galaxies in the sample, so is likely also to be the object in which we have least capability to probe the fainter regions. It could be considered a high-z Lyα-emitting analog galaxy by virtue of its luminosity and EW.

LARS 09. IRAS 0820+2816 is a very extended late-type starbursting spiral. It is also an NVSS and 5C radio source. It emits Lyα, but at the brightest UV levels is very faint, showing mostly Lyα absorption in the nucleus. A fuzz of Lyα emission is clearly visible but does not behave as an extended halo, and instead broadly traces out the optical structure. Its $L_{Ly\alpha}$ curve-of-growth is remarkable, showing Lyα in absorption in the central regions, that gets stronger out to radii of ∼3 kpc. After this radius, the curve increases very steeply until the object becomes a global Lyα emitter at $r \sim 9$ kpc. Only the growth of EW and integrated $f_{esc}^{Ly\alpha}$ are close to straight, linear growths with radius and both increase slowly. Inside the $2 \times r_{P20}$ aperture, it is a net emitter, but not a luminous one and it shows a low $W_{Ly\alpha}$ of 3 Å (and below 15 Å) at all radii. Note that a field star, coincident with the edge of the southern arm as probed by the optical images, has been masked in Figures 1 and 2.

LARS 10. Mrk 61 has the optical morphology of the later stage of a merger, showing a UV-bright core that extends over ≈5 kpc and an extended tail to the southeast. In the central few kiloparsecs, it shows a patchy, fine-scale mixture of Lyα emission and absorption, but absorbs in total within $r = 2$ kpc. In this region, Lyα EWs do not exceed around 50 Å, and Lyα/Hα ratios are found in general not to suggest re-scattering of photons in this galaxy—inside $2 \times r_{P20}$, this object shows $E_{B-V}^{neb} \approx 0.3$, and it seems likely that Lyα photons cannot escape the central regions. Some re-scattering of Lyα does occur, however, and at $r \gtrsim 5$ kpc a faint diffuse halo structure begins to emerge; the net $W_{Ly\alpha}$ within this radius is sufficient to LARS 10 a LAE analog. The rather smooth, flat, curves-of-growth suggest that much of the Lyα has been captured by roughly 12 kpc. The galaxy does have quite a high Lyα EW (≈30 Å) but is not luminous enough ($L_{Ly\alpha} \lesssim 2 \times 10^{41}$ erg s^{-1}) to be detected in Lyα at high redshift.

LARS 11. This is a highly inclined edge-on disk that extends over 40 kpc in the ultraviolet. The whole disk appears to be lit with ongoing star formation, as shown by the Hα images; the total SFR is on the order of 20–30 $M_{\odot}$ yr^{-1}, and its stellar mass is the largest in the sample. Projected on the sky with a major axis that runs SE to NW, the SE half is somewhat more active in star formation. None of the brighter star-forming regions appear to emit their Lyα directly, and instead a faint rim of Lyα emission is seen running along the lower (more southerly) edge of the disk. This may hint at some projection effect where we see only Lyα from the near side. The Lyα is clearly projected away from the UV disk, and EWs are relatively high, on the order of 100 Å. However the Lyα/Hα ratios in the same resolution elements are around 3–5 at most, which would not be indicative of strong re-scattering of photons by extended gas along this plane of

the disk. Globally we find LARS 11 to be a weakly emitting galaxy in Lyα (EW $\approx$ 7 Å) with curves-of-growth that increase slowly; the total EW is close to 20 Å, and it probably would become a LAE analog if a larger field of view (FOV) could be observed.

LARS 12. SBS 0934+547 is a UV-bright merging system. In front of the brightest star-forming regions it shows strong Lyα absorption. However, this changes to emission at $r > 2$ kpc, and the aperture-integrated Lyα measurements all increase rapidly out to $\approx$10 kpc, after which it roughly converges; a diffuse Lyα halo can be seen in the images extending over roughly this area. While very luminous in net Lyα, the EW never exceeds about 15 Å (5 Å at $2 \times r_{P20}$) and LARS 12 would not be selected as a LAE if projected to the high-z universe.

LARS 13. IRAS 0147+1254 is also a Lyman-break analog system (Hoopes et al. 2007), and is also clearly a merging system. It shows variable dust attenuations in the nebular phase which is strongly variable and scattered across the face of the object. Lyα emission is also rather patchy and varies between absorption and weak emission. Unlike LARS 12, however, this emission never becomes particularly strong and LARS 13 has no substantial halo emission component. Overall, LARS 13 emits more Lyα than it absorbs, but has both small EW (6 Å), and $f_{esc}^{Ly\alpha}$ (1%) in the $2 \times r_{P20}$ aperture.

LARS 14. LARS 14 is among the most UV luminous galaxies in the sample but has a remarkably low metallicity (12 + log(O/H) = 7.8 from the electron temperature method). It also has a moderately high SFR ($\approx$15 $M_\odot$ yr^{-1}), but the current episode of star formation is also rather low-mass, making LARS 14 by far the highest specific SFR (sSFR) galaxy in the sample. Its extremely compact morphology and strong oxygen lines classify it as a green pea galaxy (Cardamone et al. 2009). Diagnostics of [O III]/Hβ versus [O I]/Hα and [S II]/Hα place it right on the delimiting line between starburst and Seyfert systems, however, and inferred gas pressures in the central regions are found to be several orders of magnitude higher than in "ordinary" starbursts (Overzier et al. 2008, 2009). In the Lyα images it shows a very bright emission, centered upon the brightest star-forming core, and a featureless, symmetric halo of surrounding Lyα. In no region does it show Lyα in absorption. Even in the central regions it shows Lyα EW and Lyα/Hα that are close to the recombination values. Inside the $2 \times r_{P20}$ aperture it shows $\approx$4 times the Lyα luminosity of the next most luminous Lyα emitter. LARS 14 emits more Lyα photons than the rest of the sample combined. Note that in Figure 4 its luminosity has been divided by 10 so that it may be visualized.

7. COMPARISON OF LARS WITH HIGH-REDSHIFT UV SELECTIONS

We now proceed to discuss how the objects in our sample at $0.028 < z < 0.18$ would be recovered by current high-z ($\gtrsim$2) galaxy surveys.

7.1. Ultraviolet Continuum Selection

Based upon their FUV luminosities alone, our galaxies have FUV ($\lambda \sim 1400$ Å) absolute magnitudes ranging between -16.8 and -20.3. For reference the faintest bins in the UV continuum ($\lambda \sim 1700$ Å) luminosity function (LF) of Reddy & Steidel (2009) $z \sim 2$ BM/BX galaxies and $z \sim 3$ Lyman Break Galaxies (LBGs) are centered around AB $= -18.3$. Ten of the 14 LARS galaxies are bright enough to have been detected by these surveys. The brightest LARS galaxy is just 0.4 mag fainter than $M^\star$ as determined by the same $z \sim 2$ continuum surveys. However, given the evolving LF at higher redshift, the brightest object corresponds to approximately $M^\star$ at $z \approx 6$ and exceeds $M^\star$ at $z \sim 7$ and 8 (Bouwens et al. 2011).

7.2. Lyα Selection

Making a direct comparison of our sample against high-z Lyα selection is less straightforward because both flux and EW criteria need to be fulfilled. Assuming the canonical EW cut of 20 Å, within the chosen apertures, LARS contains six LAE analog galaxies (01, 02, 05, 07, 08, and 14). Every one of these objects is sufficiently compact (five have aperture radii here between 1.7 and 2.4 kpc, and only LARS 08 is notably larger) that this emission would be recovered by photometry in apertures of 1.″5 radius if they were at $z > 2$. We refer to this subsample of six galaxies as *EW20LAEs*. We note also that among our six *EW20LAEs*, five have $f_{esc}^{Ly\alpha}$ that exceeds 10%, whereas one exhibits a notably lower $f_{esc}^{Ly\alpha}$ of just 2.5% (LARS 08). Were we to cut the sample by galaxies with $f_{esc}^{Ly\alpha} > 10\%$ we would retain only these five galaxies—there are no high EW galaxies with low $f_{esc}^{Ly\alpha}$, which in principle could be produced by a simple dust screen. We refer to the subsample with $f_{esc}^{Ly\alpha} > 10\%$ as the *FESC10LAEs*.

Whether a galaxy would be found as a LAE depends also upon its flux and the design of the observation, so contrasting LARS with high-z Lyα surveys will be strongly dependent upon the assumed observational parameters and redshift. At $\langle z \rangle = 0.3$ in the *Galaxy Evolution Explorer* (*GALEX*)-selected LAE sample of Cowie et al. (2010), the faintest object has $L_{Ly\alpha} = 1.5 \times 10^{41}$ erg s^{-1}. LARS contains 10 galaxies brighter than this in Lyα, including all 6 of our *EW20LAEs*. The brightest (non-active galactic nucleus LAE in Cowie et al. (2010) has $L_{Ly\alpha} = 2.7 \times 10^{42}$ erg s^{-1}, around twice as bright as our brighter objects LARS 05 and 07, but only around half the luminosity of LARS 14.

At high-z the extremely deep $2.67 < z < 3.75$ spectroscopic survey of Rauch et al. (2008) finds galaxies as faint as 10^{-18} erg s^{-1} cm^{-2} in Lyα, corresponding to a luminosity of $\approx 7 \times 10^{40}$ erg s^{-1}: the same LARS galaxies that would have been detected by Cowie et al. (2010) would also have been found by Rauch et al. (2008). For a typical "deep" narrowband Lyα survey we adopt the depth of our own $z \sim 2$ survey (Hayes et al. 2010), which reached $L_{Ly\alpha} \approx 3 \times 10^{41}$ erg s^{-1}—we would have recovered all six of the *EW20LAEs* in LARS. Reaching $L_{Ly\alpha} = 1.3 \times 10^{42}$ erg s^{-1}, the survey of Guaita et al. (2010) would only recover LARS 14 using our $2 \times r_{P20}$ aperture photometry. However extending these apertures to 8 kpc ($\approx$1″), Guaita et al. (2010) would also recover LARS 01, 02, and 05 from the *EW20LAEs*. LARS 12 is also sufficiently luminous, but does not have high enough EW to survive most survey cuts. LARS 14 is around $L^\star$ for $z = 3.1$ LAEs (Ouchi et al. 2008) and the next two LARS galaxies are a factor of four fainter. Even LARS 14, however, is too faint to be detected by the $z = 5.7$ and 6.5 survey of Hu et al. (2010), especially given the uncertain impact that the IGM would have on the Lyα throughput from these redshifts.

When contrasting our results against high-z surveys, however, note that one would also need to account for the fact that more neutral gas may reside around galaxies with increasing z. Consequently, the surface brightness may be even more extended, which may act to render a given galaxy even less detectable.

7.3. Ultraviolet Sizes

We also draw the readers' attention to the UV sizes, reported in Column 4 of Table 1. The mean $\eta = 0.2$ Petrosian radius for the sample is ≈2.5 kpc, which is strongly influenced by four large galaxies whose radii exceed ∼4 kpc: LARS 08, 09, 11, and 13, none of which enters the subsamples of either *FESC10LAEs* of *EW20LAEs*. When computing the average sizes of the *FESC10LAEs* we obtain a value of just 0.99 kpc; less than half the average size of the full sample. We note that this finding is qualitatively consistent with that of Malhotra et al. (2012), in that LAEs are drawn from the more compact end of the size distribution of LBGs. Quantitatively Malhotra et al. (2012) find LAEs to have half-light radii close to 1.0 kpc at redshifts 2–6, which is the same as our measurement of the Petrosian radius, although converting between the two varies from galaxy to galaxy and is not straightforward, depending strongly upon how well the light profile is known. These UV sizes also match well with those reported by Cowie et al. (2011) for both Lyα-emitting and non-emitting objects selected with *GALEX*.

8. WHAT GOVERNS Lyα TRANSMISSION?

While the sample is small compared to a high-z survey, it is large compared to previous low-z *HST* Lyα studies and is also far better selected, and therefore gives us modest statistical power to examine correlation of global properties. The number of properties that may affect Lyα emission is also large, and some studies (e.g., of neutral gas contents, kinematics and covering fractions) are to be deferred until future papers. The *HST* imaging data alone, combined with the available smaller aperture optical spectroscopy from SDSS, are sufficient to derive a number of interesting quantities. Regarding Lyα output, we elect to study four quantities: the luminosity, EW, Lyα/Hα ratio, and the escape fraction $f_{\rm esc}^{\rm Ly\alpha}$ (Equation (1)). We remind the reader that all our "global" quantities are computed in apertures of twice the Petrosian radius, with $\eta = 0.2$.

In Figures 5 and 6, the uppermost panels always show Lyα luminosity on the ordinate axis. One of the most interesting features of these rows of plots is that in none of them does a systematic trend emerge between $L_{\rm Ly\alpha}$ and the quantity presented on the abscissa. Total Lyα luminosity does not correlate with any other quantity that we have measured thus far. This in itself is a particularly interesting result, since even though we know the transport of Lyα to be a complex process we would still have expected some degree of correlation with most basic quantities like FUV or Hα luminosity, over which quantities the LARS sample spans a dynamic range of 1.5 dex. The Lyα numbers presented on the ordinate axes of other three rows of Figures 5 and 6 are relative quantities—Lyα luminosity divided by FUV luminosity, Lyα/Hα, and $f_{\rm esc}^{\rm Ly\alpha}$ (Lyα/intrinsic Lyα)—and as such these trace the transmission of Lyα either absolutely (in the case of $f_{\rm esc}^{\rm Ly\alpha}$) or relative to other wavelengths (Lyα/Hα or Lyα EW). In many of these plots a number of relationships and "zones of avoidance" begin to emerge. Furthermore they seem to strengthen in the order presented: zones of avoidance are better defined in $f_{\rm esc}^{\rm Ly\alpha}$ plots than Lyα/Hα plots, which in turn are better defined than those in $W_{\rm Ly\alpha}$ plots. We recall that $W_{\rm Ly\alpha}$ on any sightline is a function of {SFH, extinction, scattering}, and Lyα/Hα is more simply a function of {extinction, scattering}; $f_{\rm esc}^{\rm Ly\alpha}$ attempts to correct also for the obscuration of Hα. Specifically we find that more Lyα is transferred in galaxies with lower $L_{\rm FUV}$, lower instantaneous SFR, higher Hα EW, lower metallicity, lower dust attenuation, and at younger ages. Cautioning at the outset that many of these quantities will be correlated, we now discuss each in turn.

8.1. FUV Luminosity

$L_{\rm FUV}$ is shown in the leftmost column of Figure 5. This is a priority high-z observable, and has been much studied previously and contrasted with Lyα (Gronwall et al. 2007; Ouchi et al. 2008). Ando et al. (2006) presented a plot demonstrating the notable absence of strong Lyα emission (high EW) at higher UV luminosities, which has since been confirmed in large samples of LBGs (Stark et al. 2010; Kornei et al. 2010) and LAEs (Kashikawa et al. 2011) and discussed as a natural consequence of extinction increasing with UV magnitude in LBGs, couple with the associated radiative transfer effects (Verhamme et al. 2008).

A number of galaxies are clearly visible with high $W_{\rm Ly\alpha}$ but faint $L_{\rm FUV}$, and five of our six *EW20LAEs* have $L_{\rm FUV} \lesssim 4 \times 10^{40}$ erg s^{-1} Å^{-1} ($M_{1500} = -19.5$ AB), while the sample of non-emitting galaxies extends to approximately four times this value. LARS 14—a strongly Lyα-emitting and UV luminous galaxy—is the only object that bucks the trend somewhat. A very similar distribution of points is also present in the Lyα/Hα and $f_{\rm esc}^{\rm Ly\alpha}$ plots, which demonstrates that this effect is not purely one related to the star formation history (SFH), but is genuinely a result of the relative transmission of Lyα. We note that the cutoff magnitude suggested by Ando et al. (2006) is 1.5 mag brighter than that remarked upon here, although given the strongly differing selection functions, which include $W_{\rm H\alpha}$, and very different cosmic epochs, it is perhaps not surprising to see qualitative but not quantitative agreement.

8.2. Star Formation Rate

FUV luminosity, as discussed in Section 8.1, traces the (possibly obscured) SFR averaged over the last ≈100 Myr; we now show the unobscured instantaneous SFR (second column of Figure 5), which we derive from dust-corrected Hα, using the calibration of Kennicutt (1998). We note that some of the SFRs, even the dust-corrected ones, listed in Table 2 are rather discrepant, and we recall that we are observing galaxies that have experienced a burst of massive star formation, with a recent significant increase of their SFR. Indeed note that the ages measured for the stellar population are generally very young, and mostly far from the ages at which the stationary level on which the SFR calibrations are based has been reached.

When considering the Lyα EW we see something that resembles the Ando et al. (2006) effect, but with $L_{\rm FUV}$ replaced by Hα SFR, as expected from the models of Garel et al. (2012). Indeed the effect is even more prominent than the comparison against $L_{\rm FUV}$, with LARS 14 falling nearer the strongly Lyα-emitting but less intensely star-forming quadrant. It is clear that higher SFR galaxies do not strongly emit Lyα, and again we caution against the use of Lyα as a general SFR indicator at high-z; in a forthcoming publication we will demonstrate how even the dust-corrected Hα-derived SFR falls significantly short of the FIR-derived value in a number of cases. All the *FESC10LAEs* exhibit SFRs below 30 $M_\odot$ yr^{-1}, and galaxies with higher SFR do not emit much Lyα. The upper right part of the diagram (high SFR, high $f_{\rm esc}^{\rm Ly\alpha}$ or $W_{\rm Ly\alpha}$) is completely avoided.

8.3. Relative Star Formation Intensity

In the third column of Figure 5 we show how Lyα quantities correlate with $W_{\rm H\alpha}$ which, since Hα traces SFR and the R-band

luminosity is a rough tracer of stellar mass, is an observable that strongly correlates with the instantaneous sSFR. Certainly no correlation is seen here, but five of the six *EW20LAEs* and all of the *FESC10LAEs* have $W_{\rm H\alpha}$ above 300 Å.

We have previously shown at $z \approx 2$ that when galaxy selection criteria extend down to very low $W_{\rm H\alpha}$ ($\gtrsim$20 Å), only around 10% of the same sample are recovered by Lyα selection using the same $W_{\rm H\alpha}$ threshold (Hayes et al. 2010). At $z \sim 0.3$ Cowie et al. (2011) remarked that Lyα emission from sources with $W_{\rm H\alpha}$ below 100 Å is rare (roughly 1%) but increases with increasing $W_{\rm H\alpha}$ (30% at EW > 100 Å; 60% at EW > 250 Å).

$W_{\rm H\alpha} > 100$ Å is a condition of the LARS selection function (Paper I), but we note that these estimates of $W_{\rm H\alpha}$ were drawn from 3″circular apertures, and are not global quantities. The 1″slitlets employed by Cowie et al. (2011) are not global either, but their galaxies have the advantage of occupying a factor of five smaller physical sampling than ours (calculated from the median redshift of the two samples). The $W_{\rm H\alpha}$ we use in this paper has been recomputed inside aperture matched *HST* images, and in a few cases $W_{\rm H\alpha}$ is reduced below the 100 Å used for selection—the minimum $W_{\rm H\alpha}$ in the sample is now 65 Å—but nevertheless the $W_{\rm H\alpha}$ of LARS galaxies is still somewhat high compared to the limits used by both Cowie et al. (2011) and Hayes et al. (2010). We therefore would expect a large fraction of LARS galaxies to show Lyα emission, which is exactly what we see.

8.4. Ultraviolet Continuum Slopes

After UV luminosity, probably the next most commonly studied high-z observable is the rest-frame color of the UV continuum (Nilsson et al. 2009; Guaita et al. 2010; Blanc et al. 2011), where it is frequently invoked as a proxy for stellar dust attenuation. The correlation between the throughput Lyα radiation and the UV continuum slope β is one of the strongest in the sample, and is shown in the fourth column of Figure 5. The six reddest galaxies ($\beta > -1.7$) suppress more than 97% of their Lyα radiation, while much spread in $W_{\rm Ly\alpha}$ and $f_{\rm esc}^{\rm Ly\alpha}$ is seen at blue UV slopes. All objects with $f_{\rm esc}^{\rm Ly\alpha} > 10\%$ show β slopes bluer than -1.8. As we will discuss in the coming sub-section, this is likely because of the correlation between the UV slope and dust content.

8.5. Stellar and Nebular Dust Attenuation

Being among the easier quantities to measure in individual galaxies, the effect of dust content on Lyα emission has been studied extensively (non-exhaustively: Atek et al. 2008, 2009; Scarlata et al. 2009; Finkelstein et al. 2009, 2011a; Pentericci et al. 2009; Kornei et al. 2010; Hayes et al. 2010; Ono et al. 2010; Cowie et al. 2011; Nakajima et al. 2012). The convergent bottom line is that measures of the relative Lyα output decrease as dust content increases, although the spread in these relationships is, as usual for Lyα, large because of the additional properties that govern the Lyα transport (see Hayes et al. 2011, for a detailed discussion). The LARS sample gives us the opportunity to study the effect of both attenuation as probed by the interstellar emission lines Hα and Hβ and also on the stellar continuum from a full fit of the SED. We do this in the fifth and sixth columns of Figure 5.

The plot of $W_{\rm Ly\alpha}$ versus nebular E_{B-V} shows little correlation: the galaxy with the highest $W_{\rm Ly\alpha}$ is effectively dust free, but the remaining five *EW20LAEs* show $E_{B-V}^{\rm neb}$ up to 0.5 mag. However a comparison of $W_{\rm Ly\alpha}$ and dust content will always be

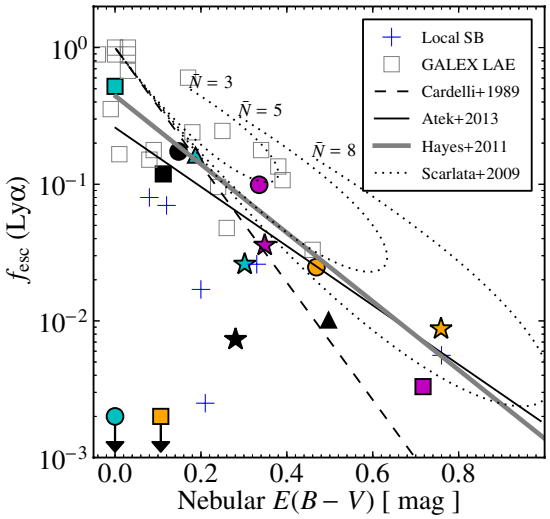

Figure 7. $f_{\rm esc}^{\rm Ly\alpha}$ vs. nebular dust attenuation E_{B-V} (always derived from Hα/Hβ) for LARS and various local galaxy samples. This is the same as Figure 5 (Column 5 row 4), but in logarithmic space. Globally absorbing galaxies are represented by upper limits, arbitrarily set to $f_{\rm esc}^{\rm Ly\alpha}$ of 0.2%. We now include the six hand-picked galaxies at $0.009 < z < 0.028$ from our local Lyα imaging pilot study (Östlin et al. 2009) with narrowband Balmer line observations (Atek et al. 2008), and 21 objects at $0.18 < z < 0.35$ selected on Lyα strength from *GALEX* slitless spectroscopy and followed up by Atek et al. (2009). The dotted line shows the $f_{\rm esc}^{\rm Ly\alpha}$ that would be expected for a pure dust-screen based upon the Cardelli et al. (1989) extinction law. The solid gray line shows the best-fitting curve to the $f_{\rm esc}^{\rm Ly\alpha}$–$E_{B-V}^{\rm stel}$ points assembled in $z = 2$–3 galaxies in Hayes et al. (2011), and rescaled to $E_{B-V}^{\rm neb}$ using the factor of 2.2 from Calzetti et al. (2000). The solid black line represents a similar fit to $f_{\rm esc}^{\rm Ly\alpha}$–$E_{B-V}^{\rm neb}$ derived for $z \sim 0.25$ LAEs (Atek et al. 2013). The black dotted lines show loci of points that would be expected for Poissonianly distributed clumps of dust, as implemented by Scarlata et al. (2009). Symbols for LARS galaxies are the same as in Figure 4. (A color version of this figure is available in the online journal.)

complicated by the fact that intrinsic EWs are a function of the SFH, and that the stellar and nebular radiation may be subject to different dust contents. Indeed when we compare instead the dust contents with Lyα/Hα ratio and $f_{\rm esc}^{\rm Ly\alpha}$, a more traditional picture emerges: the *EW20LAEs* with higher dust content tend to be among the ones with lower $f_{\rm esc}^{\rm Ly\alpha}$, and the zone-of-avoidance on the plot at high-$f_{\rm esc}^{\rm Ly\alpha}$ and high-$E_{B-V}^{\rm neb}$ becomes quite prominent: all the *FESC10* LAEs are found at lower dust content, whereas no galaxies with $E_{B-V}^{\rm neb} > 0.35$ show $f_{\rm esc}^{\rm Ly\alpha}$ above a few percent.

In Figure 7 we show a more detailed plot of $f_{\rm esc}^{\rm Ly\alpha}$ versus $E_{B-V}^{\rm neb}$, together with points from our previous studies (Atek et al. 2008, 2009). This shows how $E_{B-V}^{\rm neb}$ impacts $f_{\rm esc}^{\rm Ly\alpha}$ in samples for which we are able to match apertures, and the logarithmic scaling of the $f_{\rm esc}^{\rm Ly\alpha}$ axis illustrates the large dispersion inherent in the relationship, even when dust content is low. We have set globally Lyα-absorbing galaxies LARS 04 and 06 to an arbitrary upper limit, below the lowest $f_{\rm esc}^{\rm Ly\alpha}$ emitter. It is remarkable that even with such a small sample, $f_{\rm esc}^{\rm Ly\alpha}$ spans two orders of magnitude at low $E_{B-V}^{\rm neb}$, while galaxies with dust contents a factor of five higher are clearly emitters. For illustration, we plot as the dashed black line the $f_{\rm esc}^{\rm Ly\alpha}$ expected from pure dust-screen extinction, assuming the Cardelli et al. (1989) Galactic curve. All the galaxies at lower dust content lie below this curve, where Lyα is preferentially suppressed by H I scattering. However there is also a group of three LARS galaxies and several from the Lyα-selected samples that lie

above this curve. In solid black and gray lines, respectively, we plot the empirical $f_{\rm esc}^{\rm Ly\alpha}$–$E_{B-V}$ relationships of Atek et al. (2013), which was derived at $\langle z\rangle = 0.25$ from Hα/Hβ, and of Hayes et al. (2011) which was derived at $z = 2$–3 from SED fitting to the stellar continuum, and scaling $E_{B-V}^{\rm stel}$ to $E_{B-V}^{\rm neb}$ using the factor of 2.2 suggested by Calzetti et al. (2000). With the dotted lines we plot the global dust attenuation expected from the models of Natta & Panagia (1984), which have been advocated to explain the observed line ratios for local LAEs by Scarlata et al. (2009); see also Calzetti et al. (1994) and Charlot & Fall (2000) for more discussion of these geometries. Here $\tilde{N}$ Poissonianly distributed clumps lie along the line-of-sight, and $E_{B-V}^{\rm neb}$ is computed from the optical depth of all clumps. These three latter parameterizations are able, with reasonable accuracy, to capture the upper envelope of points in the LARS sample. Eight galaxies lie along these relationships, including all the *FESC10LAEs*. Importantly, all the six *EW20LAEs* lie along the empirical lines, which were derived in samples that were selected with precisely that selection function. Unlike the Hayes et al. and Atek et al. empirical prescriptions for Lyα, however, the clumpy dust models (Natta & Panagia 1984) were developed with concerns completely independent from Lyα, and only later applied to the *GALEX*-selected objects. The broad agreement between the models, particularly at higher levels of attenuation, may hint at their reality. It is interesting also that in the $f_{\rm esc}^{\rm Ly\alpha}$–$E_{B-V}^{\rm neb}$ plane the upper envelope of our UV-selected sample behaves very similarly to the Lyα-selected samples, at both low- and high-z.

In the UV-selected LARS sample, and also the mixed sample-selection of Atek et al. (2008) and Östlin et al. (2009) there is a sequence of points that falls away from this line. Here it is clear that Lyα must be preferentially attenuated compared to other hydrogen line radiation as H I increases the dust absorption probability or scatters Lyα to very large radii where it cannot be detected. For example LARS 09 only becomes a net Lyα emitter when large apertures are considered and it is possible that both LARS 04 and 06 would do the same if very wide field UV observations could be obtained. In Hayes et al. (2013) we discuss how Lyα becomes systematically more extended compared to the UV and Hα as dust content decreases. It is likely that in defining our apertures based upon UV sizes we are underestimating Lyα fluxes in a way that the underestimate is larger in the less dusty systems. Correcting for this would increase $f_{\rm esc}^{\rm Ly\alpha}$ more in lower E_{B-V} galaxies, and could in principle reduce the apparent dispersion in this figure. If we could assemble a very large UV-selected sample with global Lyα information we would expect the lower region of the plot at lower $f_{\rm esc}^{\rm Ly\alpha}$ and $E_{B-V}^{\rm neb}$ to be filled in. Based upon current information derived from both Lyα and UV selection, we see no evidence for stronger Lyα emission than described by the envelopes of our defined relationships, and no need for a finely tuned "scattering+shielding" radiation transport (Neufeld 1991).

8.6. Stellar Age and Mass

We show stellar age and mass in Columns 7 and 8 of Figure 5. Most observational studies of the stellar populations of Lyα galaxies suggest that they are relatively young and low-mass systems (Ono et al. 2010; Nilsson et al. 2011; Acquaviva et al. 2012), although see Finkelstein et al. (2009) for counterexamples. In addition, several theoretical studies have also predicted Lyα strength to follow evolutionary sequences (Tenorio-Tagle et al. 1999; Thommes & Meisenheimer 2005; Mao et al. 2007), although details vary. In contrast, Pentericci et al. (2009, 2010) find no correlation of Lyα EW with stellar age among LBGs, and Verhamme et al. (2008) have also noted that trends with age should not be strong in LBGs because star formation proceeds close to equilibrium, where the Lyα EW has saturated. An obvious question, therefore, is whether we see any age-dependent trends among galaxies in the LARS sample.

Looking at our six *EW20LAEs*, it seems that five of them have a preference for very young ages, while the other (the lowest $W_{\rm Ly\alpha}$ of the subsample) exhibits the oldest stellar population in the sample. However when cast by $f_{\rm esc}^{\rm Ly\alpha}$, all the seven oldest galaxies transmit below 3% of their intrinsic Lyα radiation, while all *FESC10LAEs* have ages below 10 Myr. It is curious that this timescale corresponds roughly to the ionizing lifespan of a simple stellar population (SSP), and while it makes sense for $W_{\rm Ly\alpha}$ to follow such a trend the same would not necessarily be predicted for $f_{\rm esc}^{\rm Ly\alpha}$. Scenarios could be invoked whereby a certain evolutionary time is needed to produce the dust to suppress the Lyα emission, yet the oldest galaxies are not the most dusty (Table 2). The result is also largely in tension with the scenario of Tenorio-Tagle et al. (1999) which requires a certain timescale for kinetic feedback to accelerate the neutral gas.

At high stellar masses there is also a notable deficiency of strong Lyα emitters. A declining relationship between all the relative Lyα quantities and the mass is clearly seen, and is most apparent in the figure of $f_{\rm esc}^{\rm Ly\alpha}$. There are seven galaxies with a total stellar mass below $10^{10}\,M_{\odot}$, and five of them are the *FESC10LAEs*; obviously, every galaxy above this mass limit transmits below 3% of its Lyα. These results are certainly in qualitative agreement with the hypothesis that Lyα-selection would find lower-mass systems, and radiative transport predictions for Lyα transmission (e.g., Laursen et al. 2009; Yajima et al. 2012). Current thinking suggests that this phenomenon is due to the increased gas and dust content of more massive galaxies—from direct H I observations we will soon empirically demonstrate this to be the case within the LARS sample (S. Pardy et al. in preparation).

8.7. Nebular Metallicity and Excitation

Finally we show some properties derived from SDSS spectroscopy, relating to nebular abundances and the excitation parameter, in Figure 6. Charlot & Fall (1993) presented an anti-correlation between Lyα EW and metallicity, derived from *IUE* spectroscopy and ground-based observations. Even at the time, it was easy to find local dwarf starbursts that would outlie this relatively narrow distribution by roughly 2 dex (Kunth et al. 1994; Thuan & Izotov 1997). Indeed the $W_{\rm Ly\alpha}$–Z relationship became weaker after the development of new data-reduction tools and acquisition of aperture-matched supplementary data (Giavalisco et al. 1996). However, more recently and working in a sample that was both larger and much more cleanly selected, Cowie et al. (2011) showed that indeed Lyα-emitting galaxies have metallicities systematically lower than UV-selected galaxies of similar continuum magnitude that show no Lyα emission. Note here that in contrast to Giavalisco et al. (1996) the Lyα and optical apertures are not matched, but the UV does encompass all the Lyα. Our case is similar—the Lyα fluxes may be close to global, but the metallicities are derived from smaller SDSS fibers. Piecemeal results at high-z have also found strongly Lyα-emitting galaxies to be of systematically low metallicity (Fosbury et al. 2003; Erb et al.

2010; Finkelstein et al. 2011b; Nakajima et al. 2012; Guaita et al. 2013), and also with high ionization parameter (Nakajima et al. 2013).

From the SDSS spectra we examine four quantities that are frequently used to quantify nebular properties at low-z, and are now emerging as diagnostics of galaxies at $z = 2$–3. These include the R_{23} index [$\equiv$ ([O II] 3727+[O III] 4959+[O III] 5007)/Hβ]; the $N2$ index [$\equiv$ log([N II] 6584/Hα)]; the excitation parameter, P [$\equiv$ [O III] 4959, 5007/([O II] 3727+[O III] 4959, 5007)]; and a strong-line metallicity, for which we adopt the O3N2 method and the calibration of Yin et al. (2007). All these quantities, and the spectroscopic fluxes from which they were derived, can be found in Paper I. With the large current investment in NIR followup of high-z galaxies and new high-multiplexing NIR spectrographs, we can expect a lot more such measurements to be published in the coming years.

Trends are visible between $W_{\rm Ly\alpha}$ and all four of the above listed nebular quantities, with strongly Lyα-emitting galaxies exhibiting lower $N2$, and metallicity, and higher R_{23} and P. Once again, trends appear stronger when cast as $f_{\rm esc}^{\rm Ly\alpha}$, and all *FESC10LAEs* are found to exhibit low [N II]/Hα ratios, high oxygen/Hβ ratios, and high [O III]/[O II] ratios. All of these three quantities are correlated with each other and also with the nebular metallicity, but curiously the trend with O3N2-determined oxygen abundance is the weakest in Figure 6. While at least plausibility may be invoked for a relationship with Z—e.g., metal abundance correlates with dust abundance and suppresses Lyα—it is not clear why the relationships with R_{23}, P, and $N2$ should be tighter. Taken at face-value, it appears that a hotter stellar population is needed not only to produce Lyα photons but also to facilitate their escape.

8.8. Summary

To summarize this section, we note briefly that we find no relationship between total Lyα luminosity and any of the secondary galaxy properties we have tested here. When considering the Lyα EW, however, some trends begin to emerge, but they are seen more clearly when examining direct nebular relative measurements for Lyα: Lyα/Hα and $f_{\rm esc}^{\rm Ly\alpha}$. We find Ly$\alpha$ transmission to be higher at lower $L_{\rm FUV}$, lower intrinsic instantaneous SFR, higher $W_{\rm H\alpha}$, bluer UV continuum colors, lower dust attenuation, younger ages, lower stellar masses, lower $N2$ and metallicity, and higher R_{23} and excitation parameter. Of course these are just observational considerations—we do not claim that all of these effects form a direct causal relation nor that these quantities are uncorrelated. Clearly many of them will be.

9. SUMMARY AND CONCLUSIONS

The Lyman Alpha Reference Sample comprises 14 galaxies at redshift between 0.028 and 0.18 in which the dominant source of ionization is determined to be star formation (Paper I). In this article we have presented individual images obtained with the *HST* in the FUV continuum, Hα, and Lyα, and maps of the ratios of Hα/Hβ, Lyα/Hα, and Lyα/FUV (i.e., the Lyα EW). From the intensity maps we have produced radial light profiles in Lyα, Hα, and the FUV, and photometric aperture curves-of-growth for Lyα, FUV, $W_{\rm Ly\alpha}$, and $f_{\rm esc}^{\rm Ly\alpha}$. We have defined standardized apertures, and computed a number of global properties of the sample, including aperture-matched quantities that describe the Lyα output and also the properties of the nebular gas and massive stellar population. We find the following.

1. The morphology of Lyα is usually very different from the Hα and FUV morphologies, and that many features seen in Hα are not visible in Lyα. We interpret this, together with the large, extended Lyα haloes that we have presented previously (Hayes et al. 2013), as the scattering of Lyα photons in the neutral ISM that surrounds the star-forming regions. This is supported by the observed line ratios that exceed the case B values by factors of more than three.
2. Radial profiles in Lyα are flatter than those of the UV continuum, and exhibit Sérsic indices that are systematically lower in Lyα than the UV. Moreover, radial profiles in $W_{\rm Ly\alpha}$ and Lyα/Hα often exceed their intrinsic recombination values by large factors, even in complete radial annuli. These two observations demonstrate the spatial redistribution of Lyα to large radii as a result of H I scattering.
3. Photometric growth curves rise more slowly in Lyα than in the UV and Hα. We caution that in some cases there may be unpredictable, and possibly substantial aperture-dependencies and systematic effects involved in the measurement of these quantities in high-z samples, at least with "normal" apertures of 1″–2″. These cases, however, do not appear to be in the majority in our sample, at least within the limits of the available FOV.
4. Some regions of locally enhanced Lyα emission coincide with filamentary structures in the nebular gas. This could easily be explained by outflows that become Rayleigh–Taylor unstable and fragment, thereby increasing the Lyα flow in these directions because of a reduced covering fraction and increased velocity offset in the neutral gas.
5. Ten of our fourteen galaxies are analogous in luminosity to high-z Lyman-break galaxies, and six could be detected by deep Lyα narrowband surveys that select objects with $W_{\rm Ly\alpha}$ above 20 Å. We find five galaxies to have high Lyα escape fractions (above 10%), with the remaining nine showing $f_{\rm esc}^{\rm Ly\alpha}$ below 3%. Several of these strongly emitting galaxies are indeed bright, showing EWs above 60 Å in two cases and in one case—LARS 02—a $f_{\rm esc}^{\rm Ly\alpha}$ of 75% at radius of just a few kpc. Such values have not previously been reported in nearby galaxies, and appear also to be rare at high-z. This object may be a very interesting laboratory for detailed study.
6. Lyα throughput (EW, Hα ratio, $f_{\rm esc}^{\rm Ly\alpha}$) is systematically higher in galaxies of faint FUV magnitude, lower SFR, higher Hα EW, bluer UV colors, lower extinction, lower mass, and nebular quantities that suggest more intense UV radiation fields. In contrast, we have not yet found Lyα luminosity to correlate strongly with any of the quantities we have measured.

M.H. acknowledges support from the Swedish research council (VR) and the Swedish National Space Board (SNSB) and also received support from Agence Nationale de la recherche bearing the reference ANR-09-BLAN-0234-01. G.Ö. is a Swedish Royal Academy of Sciences research fellow supported by a grant from Knut and Alice Wallenberg foundation, and also acknowledges support from the Swedish research council (VR) and the Swedish National Space Board (SNSB). A.V. benefits from the fellowship "Boursière d'excellence de l'Université de Genève." I.O. was financed through the Sciex fellowship by the Rectors' Conference of Swiss Universities. H.A. and D.K. are supported by the Centre National d'Études Spatiales

(CNES) and the Programme National de Cosmologie et Galaxies (PNCG). P.L. acknowledges support from the ERC-StG grant EGGS-278202. H.O.F. acknowledges financial support from CONACYT grant 129204, Spanish FPI grant BES-2006-13489, and was also financed through a postdoctoral UNAM grant. H.O.F. and J.M.M.H. are funded by Spanish MINECO grants AYA2010-21887-C04-02 (ESTALLIDOS), AYA2011-24780/ESP, and AYA2012-39362-C02-01.

Facilities: HST (ACS,WFC3).

REFERENCES

Acquaviva, V., Vargas, C., Gawiser, E., & Guaita, L. 2012, ApJL, 751, L26
Ando, M., Ohta, K., Iwata, I., et al. 2006, ApJL, 645, L9
Asplund, M., Grevesse, N., Sauval, A. J., & Scott, P. 2009, ARA&A, 47, 481
Atek, H., Kunth, D., Hayes, M., Östlin, G., & Mas-Hesse, J. M. 2008, A&A, 488, 491
Atek, H., Kunth, D., Schaerer, D., et al. 2009, A&A, 506, L1
Atek, H., Kunth, D., Schaerer, D., et al. 2013, A&A, in press (arXiv:1308.6577)
Bertin, E., & Arnouts, S. 1996, A&AS, 117, 393
Blanc, G. A., Adams, J. J., Gebhardt, K., et al. 2011, ApJ, 736, 31
Bouwens, R. J., Illingworth, G. D., Oesch, P. A., et al. 2011, ApJ, 737, 90
Calzetti, D., Armus, L., Bohlin, R. C., et al. 2000, ApJ, 533, 682
Calzetti, D., Kinney, A. L., & Storchi-Bergmann, T. 1994, ApJ, 429, 582
Cappellari, M., & Copin, Y. 2003, MNRAS, 342, 345
Cardamone, C., Schawinski, K., Sarzi, M., et al. 2009, MNRAS, 399, 1191
Cardelli, J. A., Clayton, G. C., & Mathis, J. S. 1989, ApJ, 345, 245
Charlot, S., & Fall, S. M. 1993, ApJ, 415, 580
Charlot, S., & Fall, S. M. 2000, ApJ, 539, 718
Cooper, J. L., Bicknell, G. V., Sutherland, R. S., & Bland-Hawthorn, J. 2008, ApJ, 674, 157
Cowie, L. L., Barger, A. J., & Hu, E. M. 2010, ApJ, 711, 928
Cowie, L. L., Barger, A. J., & Hu, E. M. 2011, ApJ, 738, 136
Diehl, S., & Statler, T. S. 2006, MNRAS, 368, 497
Dijkstra, M., & Jeeson-Daniel, A. 2013, MNRAS, 435, 3333
Dijkstra, M., Wyithe, J. S. B., & Haiman, Z. 2007, MNRAS, 379, 253
Erb, D. K., Pettini, M., Shapley, A. E., et al. 2010, ApJ, 719, 1168
Feldmeier, J. J., Hagen, A., Ciardullo, R., et al. 2013, ApJ, 776, 75
Finkelstein, S. L., Cohen, S. H., Moustakas, J., et al. 2011a, ApJ, 733, 117
Finkelstein, S. L., Hill, G. J., Gebhardt, K., et al. 2011b, ApJ, 729, 140
Finkelstein, S. L., Rhoads, J. E., Malhotra, S., & Grogin, N. 2009, ApJ, 691, 465
Fosbury, R. A. E., Villar-Martín, M., Humphrey, A., et al. 2003, ApJ, 596, 797
France, K., Nell, N., Green, J. C., & Leitherer, C. 2010, ApJL, 722, L80
Fruchter, A., & Sosey, M. 2009, The MultiDrizzle Handbook, version 3.0 (Baltimore, MD: STScI)
Fynbo, J. U., Möller, P., & Thomsen, B. 2001, A&A, 374, 443
Garel, T., Blaizot, J., Guiderdoni, B., et al. 2012, MNRAS, 422, 310
Giavalisco, M., Koratkar, A., & Calzetti, D. 1996, ApJ, 466, 831
Gonzaga, S., et al. 2011, ACS Data Handbook, version 6.0 (Baltimore, MD: STScI)
González Delgado, R. M., Leitherer, C., & Heckman, T. M. 1999, ApJS, 125, 489
Gronwall, C., Ciardullo, R., Hickey, T., et al. 2007, ApJ, 667, 79
Guaita, L., Francke, H., Gawiser, E., et al. 2013, A&A, 551, A93
Guaita, L., Gawiser, E., Padilla, N., et al. 2010, ApJ, 714, 255
Haiman, Z., & Spaans, M. 1999, ApJ, 518, 138
Hayes, M., Östlin, G., Atek, H., et al. 2007, MNRAS, 382, 1465
Hayes, M., Östlin, G., Mas-Hesse, J. M., & Kunth, D. 2009, AJ, 138, 911
Hayes, M., Östlin, G., Mas-Hesse, J. M., et al. 2005, A&A, 438, 71
Hayes, M., Östlin, G., Schaerer, D., et al. 2010, Natur, 464, 562
Hayes, M., Östlin, G., Schaerer, D., et al. 2013, ApJL, 765, L27
Hayes, M., Schaerer, D., Östlin, G., et al. 2011, ApJ, 730, 8
Heckman, T. M., Borthakur, S., Overzier, R., et al. 2011, ApJ, 730, 5
Hoopes, C. G., Heckman, T. M., Salim, S., et al. 2007, ApJS, 173, 441
Hopkins, A. M., & Beacom, J. F. 2006, ApJ, 651, 142
Hu, E. M., Cowie, L. L., Barger, A. J., et al. 2010, ApJ, 725, 394
Hummer, D. G., & Storey, P. J. 1987, MNRAS, 224, 801
Kashikawa, N., Shimasaku, K., Malkan, M. A., et al. 2006, ApJ, 648, 7
Kashikawa, N., Shimasaku, K., Matsuda, Y., et al. 2011, ApJ, 734, 119
Kennicutt, R. C., Jr. 1998, ARA&A, 36, 189
Kornei, K. A., Shapley, A. E., Erb, D. K., et al. 2010, ApJ, 711, 693
Kulas, K. R., Shapley, A. E., Kollmeier, J. A., et al. 2012, ApJ, 745, 33
Kunth, D., Lequeux, J., Sargent, W. L. W., & Viallefond, F. 1994, A&A, 282, 709
Kunth, D., Mas-Hesse, J. M., Terlevich, E., et al. 1998, A&A, 334, 11
Laursen, P., Sommer-Larsen, J., & Andersen, A. C. 2009, ApJ, 704, 1640
Lidman, C., Hayes, M., Jones, D. H., et al. 2012, MNRAS, 420, 1946
Mac Low, M.-M., & McCray, R. 1988, ApJ, 324, 776
Malhotra, S., & Rhoads, J. E. 2004, ApJL, 617, L5
Malhotra, S., Rhoads, J. E., Finkelstein, S. L., et al. 2012, ApJL, 750, L36
Mao, J., Lapi, A., Granato, G. L., de Zotti, G., & Danese, L. 2007, ApJ, 667, 655
Mas-Hesse, J. M., Kunth, D., Tenorio-Tagle, G., et al. 2003, ApJ, 598, 858
Matsuda, Y., Yamada, T., Hayashino, T., et al. 2012, MNRAS, 425, 878
Nakajima, K., Ouchi, M., Shimasaku, K., et al. 2012, ApJ, 745, 12
Nakajima, K., Ouchi, M., Shimasaku, K., et al. 2013, ApJ, 769, 3
Natta, A., & Panagia, N. 1984, ApJ, 287, 228
Neufeld, D. A. 1991, ApJL, 370, L85
Nilsson, K. K., Östlin, G., Møller, P., et al. 2011, A&A, 529, A9
Nilsson, K. K., Tapken, C., Møller, P., et al. 2009, A&A, 498, 13
Ono, Y., Ouchi, M., Shimasaku, K., et al. 2010, MNRAS, 402, 1580
Osterbrock, D. E. 1989, Astrophysics of Gaseous Nebulae and Active Galactic Nuclei (Mill Valley, CA: Univ. Science Books)
Östlin, G., Hayes, M., Kunth, D., et al. 2009, AJ, 138, 923
Otí-Floranes, H., Mas-Hesse, J. M., Jiménez-Bailón, E., et al. 2012, A&A, 546, A65
Ouchi, M., Shimasaku, K., Akiyama, M., et al. 2008, ApJS, 176, 301
Overzier, R. A., Heckman, T. M., Kauffmann, G., et al. 2008, ApJ, 677, 37
Overzier, R. A., Heckman, T. M., Tremonti, C., et al. 2009, ApJ, 706, 203
Partridge, R. B., & Peebles, P. J. E. 1967, ApJ, 147, 868
Pentericci, L., Grazian, A., Fontana, A., et al. 2009, A&A, 494, 553
Pentericci, L., Grazian, A., Scarlata, C., et al. 2010, A&A, 514, A64
Petrosian, V. 1976, ApJL, 209, L1
Prevot, M. L., Lequeux, J., Prevot, L., Maurice, E., & Rocca-Volmerange, B. 1984, A&A, 132, 389
Quider, A. M., Pettini, M., Shapley, A. E., & Steidel, C. C. 2009, MNRAS, 398, 1263
Raiter, A., Schaerer, D., & Fosbury, R. A. E. 2010, A&A, 523, A64
Rauch, M., Haehnelt, M., Bunker, A., et al. 2008, ApJ, 681, 856
Reddy, N. A., & Steidel, C. C. 2009, ApJ, 692, 778
Rhoads, J. E., Dey, A., Malhotra, S., et al. 2003, AJ, 125, 1006
Santos, M. R. 2004, MNRAS, 349, 1137
Scarlata, C., Colbert, J., Teplitz, H. I., et al. 2009, ApJL, 704, L98
Schaerer, D. 2003, A&A, 397, 527
Schaerer, D., de Barros, S., & Stark, D. P. 2011, A&A, 536, A72
Shapley, A. E., Steidel, C. C., Pettini, M., & Adelberger, K. L. 2003, ApJ, 588, 65
Shapley, A. E., Steidel, C. C., Pettini, M., Adelberger, K. L., & Erb, D. K. 2006, ApJ, 651, 688
Shimasaku, K., Kashikawa, N., Doi, M., et al. 2006, PASJ, 58, 313
Stark, D. P., Ellis, R. S., Chiu, K., Ouchi, M., & Bunker, A. 2010, MNRAS, 408, 1628
Stark, D. P., Ellis, R. S., & Ouchi, M. 2011, ApJL, 728, L2
Steidel, C. C., Adelberger, K. L., Shapley, A. E., et al. 2003, ApJ, 592, 728
Steidel, C. C., Bogosavljević, M., Shapley, A. E., et al. 2011, ApJ, 736, 160
Tapken, C., Appenzeller, I., Noll, S., et al. 2007, A&A, 467, 63
Tenorio-Tagle, G., Silich, S. A., Kunth, D., Terlevich, E., & Terlevich, R. 1999, MNRAS, 309, 332
Thommes, E., & Meisenheimer, K. 2005, A&A, 430, 877
Thuan, T. X., & Izotov, Y. I. 1997, ApJ, 489, 623
Valls-Gabaud, D. 1993, ApJ, 419, 7
Vanzella, E., Grazian, A., Hayes, M., et al. 2010, A&A, 513, A20
Verhamme, A., Schaerer, D., Atek, H., & Tapken, C. 2008, A&A, 491, 89
Wofford, A., Leitherer, C., & Salzer, J. 2013, ApJ, 765, 118
Yajima, H., Li, Y., Zhu, Q., et al. 2012, arXiv:1209.5842
Yamada, T., Matsuda, Y., Kousai, K., et al. 2012, ApJ, 751, 29
Yin, S. Y., Liang, Y. C., Hammer, F., et al. 2007, A&A, 462, 535